Chemical Engineering Journal 514 (2025) 162887

Contents lists available at ScienceDirect

Chemical Engineering Journal

journal homepage: www.elsevier.com/locate/cej

Platinum interlayers reduce charge transport barriers between amorphous Ir-oxide OER electrocatalysts and the porous transport layer☆

Moritz Geuß [a,b,*], Lukas Löttert [a,b], Andreas Hutzler [a], Julian Schwarz [c], Jaroslava Nováková [d], Ivan Khalakhan [d], Miran Gaberšček [e], Karl J.J. Mayrhofer [a,b], Simon Thiele [a,b], Serhiy Cherevko [a,*]

[a] Helmholtz Institute Erlangen-Nürnberg for Renewable Energy (IET-2), Forschungszentrum Jülich GmbH, Cauerstr. 1, 91058 Erlangen, Germany
[b] Department of Chemical and Biological Engineering, Friedrich-Alexander-Universität Erlangen-Nürnberg, Immerwahrstr. 2a, 91058 Erlangen, Germany
[c] Electron Devices, Friedrich-Alexander-Universität Erlangen-Nürnberg, Cauerstr. 6, 91058 Erlangen, Germany
[d] Department of Surface and Plasma Science, Faculty of Mathematics and Physics, Charles University, V Holešovičkách 2, 180 00 Praha 8, Czech Republic
[e] National Institute of Chemistry, Department of Materials Chemistry, Hajdrihova ulica 19, 1000 Ljubljana, Slovenia

ARTICLE INFO

Keywords:
Proton exchange membrane water electrolysis
Gas diffusion electrode
Oxygen evolution reaction
Schottky junction
Impedance spectroscopy

ABSTRACT

Significant research efforts are dedicated to reducing the iridium loading in proton-exchange membrane water electrolyzers. Recently, the focus shifted toward better understanding the interplay between the titanium porous transport layers (PTLs) and the Ir-oxide-based catalyst layers, where significant performance losses were observed for low-loaded anodes based on intrinsically highly active but poorly conductive amorphous IrO_x. In the presented study, a gas-diffusion electrode half-cell setup is used to promote an understanding of the underlying phenomena leading to this low performance. The influence of the PTL platinization on the performance of realistic porous transport electrodes (PTEs) for the oxygen evolution reaction (OER) is investigated by gradually increasing the platinum layer thickness for PTEs based on amorphous and rutile Ir-oxide. Electrochemical measurements show a beneficial influence of platinization on the activity for amorphous, but not for rutile Ir-oxide. Impedance analysis corroborates the formation of a Schottky-type interface between the PTL and the amorphous IrO_x catalyst layers, depending on the PTL's platinum layer thickness. We presume that this heterogeneous Schottky-type interface induces an additional voltage drop and influences the utilization of the catalyst layer, leading to increased overpotentials. The measurements were complemented by inductively coupled plasma mass spectrometry showing constant integral amounts of Ir dissolving from the catalyst layers during the OER, independent of the platinization. Transferring the obtained knowledge to single cells, the whole composite anode, including e.g. the interplay between PTL and catalyst layer, must be optimized in conjunction to achieve optimum OER performance and long-term stability.

1. Introduction

In 2023, the increasing utilization of renewable energy sources led to a pronounced increase in negative electricity sales prices in the European Union.[1] Proton exchange membrane water electrolysis (PEMWE) is a promising technique to buffer this excess in electricity supply, especially due to its adaptability to a fluctuating power supply.[2] Since the costs for other stack components, notably bipolar plates,[3] were reduced significantly in recent years, e.g., by considering the utilization of economically viable materials like stainless steel instead of Ti,[4] the catalyst coated membrane (CCM) is currently considered the most significant contributor to the stack capital cost.[5] Given the high scarcity and price of iridium, even compared to platinum used on the cathode, reducing the Ir loading on the anode is promising to reduce CCM- and thus stack-costs.[6].

State-of-the-art Ir loadings are in the range of 1 – 3 mg_{Ir} cm^{-2},[3] while recent publications successfully showed the reduction of the anodic catalyst loading to values below 0.3 mg_{Ir} cm^{-2} using advanced

☆ This article is part of a special issue entitled: 'HYCELTEC2024' published in Chemical Engineering Journal.

* Corresponding authors at: Helmholtz Institute Erlangen-Nürnberg for Renewable Energy (IET-2), Forschungszentrum Jülich GmbH, Cauerstr. 1, 91058 Erlangen, Germany.
E-mail addresses: m.geuss@fz-juelich.de (M. Geuß), s.cherevko@fz-juelich.de (S. Cherevko).

https://doi.org/10.1016/j.cej.2025.162887

Available online 21 April 2025

catalyst layer (CL) preparation techniques, [7–9] or supported Ir-oxides. [10,11] The anodic catalyst layers are contacted by porous transport layers (PTLs) based on sintered titanium (Ti) powder or fibers to maintain electrical and thermal conductivity between the anodic catalyst layers and the flow field and to facilitate the mass transport of water and gaseous O_2.[12] In contrast to carbon-based gas-diffusion layers (GDLs) used in proton exchange membrane fuel cells (PEMFC) or as support for the cathode of PEM electrolyzers, these Ti-PTLs commonly do not contain a microporous layer.[13] Hence, the anodic catalyst layer is in direct contact with the pores of the Ti-PTL, which usually exhibit diameters > 10 μm.[12,14] Due to the large pore sizes of the Ti-PTLs, parts of the CL are not in direct contact with the PTL and are only electrically connected via the in-plane electronic conductivity of the catalyst layer.[15] When manufacturing the above-mentioned low-loaded catalyst layers, the thickness of the catalyst layers decreases with the decrease in loading. Depending on the preparation method, e.g., Mayer-rod coating,[10] spray-coating,[8] or reactive spray deposition, [7] below a certain thickness, the catalyst layer's homogeneity and in-plane electronic conductivity are compromised.[11,15] Therefore, an Ir loading reduction in combination with standard Ti-PTLs can lead to the insulation of parts of the catalyst layer and reduced catalyst utilization.[16,17] Cross-section scanning transmission electron microscopy (STEM) imaging also suggests that this inhomogeneous utilization of the catalyst layer leads to increased degradation in areas that are directly in contact with the PTL and thus subject to higher oxygen evolution reaction (OER) currents.[18] Additionally, the conditions during electrolyzer operation can influence the interplay between the PTL and the CL. A three-electrode single-cell study showed that a transition of an initially rutile IrO_2/TiO_2 catalyst toward hydrous Ir-oxide – due to H_2 crossover and the reduction of the catalyst surface during idle periods – led to an increased contact resistance between the PTL and the CL and, hence, decreasing cell performance.[19].

There are different approaches to increasing the catalyst utilization at low loadings. Improved cell performances were reported by introducing Ti microporous layers between regular Ti-PTLs and low-loaded CCMs ($0.2 - 0.4$ mg_{Ir} cm^{-2}).[20,21] In another study, an interfacial IrO_x nanofiber layer was introduced between the Ti-PTL and the CL.[22] The improved cell performance was attributed, among other things, to the good electronic conductivity of the interlayer, increasing catalyst utilization. Bernt *et al.* reduced the Ir loading by using supported amorphous Ir-oxide (45 wt% Ir) on titanium oxide.[10] Improved cell performances were only observed when a platinized Ti-PTL was used to avoid the passivation of the bare Ti PTL, or the catalyst was annealed to form crystalline, more conductive IrO_2.[10,23] In both cases, the interfacial contact resistance between the bare, passivated Ti PTL and the less conductive amorphous Ir-oxide was reduced, improving the cell performance significantly. Recently, Doo *et al.*[24] thoroughly investigated the interface between the Ti PTL and Ir-based catalyst layers. They concluded that the high work function of amorphous IrO_x, in combination with intimate ionomer contact on the native TiO_x layer, led to band bending and low electron conductivity across the CL|PTL interface.

Analogous to studies focusing on the influence of the CL|PTL interface, the influence of the current-collecting backing electrodes on catalyst activity was also investigated in aqueous model systems (AMS). Geiger *et al.*[25] showed that metallic Ir particles' activity and long-term polarization behavior depend on the used substrate (gold, glassy carbon, boron-doped diamond, or fluorine-doped tin oxide). A purely electrochemical evaluation of catalyst degradation was deemed insufficient since the apparent deactivation of the catalyst was attributed to the passivation of the different substrates. If more sophisticated accelerated stress tests (ASTs) are used to predict catalyst stability, the influence of the AST's potential limit on the dissolution and passivation of different supports must be considered when investigating catalyst stability.[26] Another AMS study showed that the poor electronic conductivity of MoS_2 and high contact resistance between the catalyst and the used glassy carbon backing electrode reduce the catalysts' utilization and measured hydrogen evolution activity.[27] Mixing the catalyst powder with conductive but inactive carbon improved the activity, showcasing the importance of well-conducting electrodes.

The significance of the interface between the PTL and CL in single-cell electrolyzers, as well as between the backing electrode and CL in aqueous model systems, was shown in various studies. In the presented study, we investigate the influence of Pt interlayers sputter-coated onto commercially available Ti PTLs on the OER performance of porous transport electrodes (PTEs) based on amorphous and rutile Ir-oxides. A GDE-type half-cell setup, introduced previously for evaluating OER catalysts,[28,29] is used to examine different Pt loadings between the PTL and the CL. Polarization curves and impedance spectroscopy probe the OER activity of the PTEs and the characteristics of the CL|PTL interface. As described in our previous publication,[30] Ir dissolution from the catalyst layers is traced throughout the electrochemical protocol by taking aliquots from the liquid electrolyte and the anodic water supply.

2. Experimental

2.1. PTE manufacturing

The PTEs were manufactured similarly as already described in our previous study.[30] Firstly, the PTLs were obtained by laser cutting a Ti fiber sinter material (NV Bekaert SA, 2GDL40-1.0, 56 % porosity, 1 mm thickness) to ∅ 22 mm rounds. The cleaning of the fiber sinter was conducted by successive ultrasonication for 10 min in an alkaline cleaning solution (Borer Chemie AG, Deconex OP153, 5 vol% in DI water), in Isopropanol (IPA), and in DI water. The platinization of the PTLs was conducted by sputter coating only onto the fiber sinter's front side (CL|PTL interface) after drying the PTLs at ambient conditions overnight. A magnetron sputtering device (Cressington Scientific Instruments, 108manual) was used to deposit the Pt layers at a current of 20 mA and a pressure of 4 Pa. The loading of the Pt layers was determined by weighing (Sartorius AG, Cubis, ±0.001 mg) the PTLs before and after certain sputtering times.

For spray-coating the CLs, an ink consisting of 1 wt% of solids in a solvent mixture of 50 wt% DI water and 50 wt% IPA was prepared based on previous publications.[31] The ink's ionomer content was 8 wt% total solid content. For preparation, the catalyst powder (Umicore SA, Elyst Ir75 0480, 76.42 wt% IrO_2 on TiO_2, here labeled *IrO_2/TiO_2*, or Alfa Aesar, Premion Iridium(IV)oxide, here labeled *IrO_x*), was mixed with DI water in a 100 ml glass Schott bottle. In a second vessel, IPA and Nafion D2021 solution were mixed and directly added to the catalyst. Afterward, the obtained ink was homogenized in an ice bath using an ultrasonic horn (Hielscher Ultrasonics GmbH) at a power density of 1.33 W g_{ink}^{-1} for 3×10 min followed by stirring overnight. Right before spray coating, the ink was ultrasonicated again for 3×10 min.

The spray coating was conducted using an automated coating device (SonoTek Corporation, ExactaCoat) with an ultrasonic AccuMist nozzle (48 kHz) and the heating plate set top 120 °C based on a published coating protocol.[31] Concentrical masks were used to restrict the CL area to ∅ 8 mm (0.5 cm^2 active area) in the center of the ∅ 22 mm PTLs, as described earlier.[30] The PTEs' target loading of 1 mg_{Ir} cm^{-2} was determined by the sprayed catalyst mass (Sartorius AG, Cubis, ±0.001 mg). To determine the final binder content in the prepared CLs, thermogravimetric analysis was conducted (TGA, PerkinElmer, Inc., TGA 8000) at a heating rate of 10 K min^{-1} in synthetic air up to 1000 °C, with a hold time of 30 min.[32].

A Nafion membrane (Frontis Energy, NR212, thickness 51 μm) was hot-pressed (Collin Lab & Pilot Solutions GmbH, Lab•Line P 200 S) directly on top of the CL at 160 °C and 2.5 MPa for 5 min to separate liquid electrolyte and anodic water compartment in the half-cell setup. The PTE and the membrane were sandwiched between pressure equalization pads (Pacothane Technologies, PacoPads) and Kapton tape to improve the hot-pressing quality.

2.2. Electrochemical measurements

For the electrochemical evaluation of the PTEs, a GDE half-cell setup, originally developed by Ehelebe *et al.*,[33] was modified slightly.[30] DI water was supplied as a reactant via a peristaltic pump. The active area of the electrodes was reduced from 2 cm^2 to 0.5 cm^2 to reduce the overall O_2 bubble formation at higher current densities. Nafion membranes were hot pressed on top of the CL (as described above) to minimize the crossover of the liquid electrolyte and achieve a proper ionic connection.[34].

Flat Viton sealings with ∅ 9 mm were used to seal the working electrode's (WE) sides. The WE was connected to the potentiostat (Biologic, VMP–300, 4 A booster board) by a platinum-plated titanium serpentine flow field, acting as a current collector. The connection of the reference electrode (RE, Gaskatel GmbH, HydroFlex Hydrogen Reference electrode) was established via a Luggin capillary. Pristine non-hydrophobized gas-diffusion layers (Freudenberg, E20), or a platinized mesh (Metakem GmbH, expanded sheet of Pt on Ti) were used as counter electrodes (CE). Purging of the electrolyte and water compartment individually with Ar was possible (Air Liquide S.A., 99.998 %).

The half-cell components of the GDE setup were boiled in DI water before each experiment to avoid cell contamination. Additionally, in between different catalysts, the cell was boiled in 1 wt% HNO_3 (Merck KGaA, Suprapure, 65 wt%, diluted with DI water) and subsequently three times in DI water. The half-cell components were stored submerged completely in DI water. 1 M $HClO_4$ (Merck KGaA, Normapure, 70 wt%, diluted with DI water) was used as the electrolyte for the half-cell measurements.

The electrochemical protocol is summarized in Table S 1. The protocol was initiated by 40 fast CVs (200 mV s^{-1}) to clean the samples, followed by three CVs at 50 mV s^{-1} for the initial characterization. The samples were conditioned by holding at 1 A cm^{-2} for 30 min, followed by conducting 3 polarization curves from 300 – 1000 mA cm^{-2}. Then, samples were characterized again by conducting 3 CVs at 50 mV s^{-1}. Subsequently, three holds were conducted at 200 mA cm^{-2}, 500 mA cm^{-2}, and 1 A cm^{-2} for 20 min each. To quantify the amount of dissolved Ir in the anodic water cycle and the liquid electrolyte, 2 ml samples of the respective liquids were taken at OCP after the holds. The counter electrodes, consisting of pristine non-hydrophobized carbon sheets, were replaced after each hold and digested in concentrated aqua regia after the measurement. The samples of the anodic water cycle, the liquid electrolyte, and the digested counter electrodes were later analyzed via ICP-MS to quantify Ir concentrations. The sample of the anodic water cycle was additionally investigated via IEC to determine the amount of cross-over ClO_4^-. For further information, we refer to the section on external analytics, the electrochemical protocol in Table S 1, and our previous publication.[34] After the hold at 1 A cm^{-2}, the CE was replaced by a platinized Ti-mesh, and a polarization curve was recorded between 1 mA cm^{-2} and 1000 mA cm^{-2}. Finally, three CVs at 50 mV s^{-1} were recorded again for the electrochemical surface characterization at the end of the protocol. The liquid samples and carbon sheets CEs were later analyzed via inductively coupled plasma mass spectrometry (ICP-MS, PerkinElmer, NexION 350X) and ion-exchange chromatography (IEC, Thermo Fisher Scientific Inc., Dionex ICS-5000$^+$ DP).

All samples were investigated under ambient pressure (101 kPa) at 25°C. A Pt wire, bubbled with H_2 in the used electrolyte was utilized to determine the RE potential vs. RHE. Ultrapure liquid water (Merck, Milli-Q) was supplied to the backside of the PTL with a flowrate of 2 ml min^{-1} cm^{-2}. The volume in the water cycle and the liquid electrolyte were 120 ml H_2O and 120 ml 1 M $HClO_4$, respectively.

2.3. External analytics

ICP-MS was used to quantify the amount of Ir in the samples taken during the electrochemical protocol. Standard solutions were prepared containing a known amount of Ir (0, 0.1, 0.5, 1, 5 μg l^{-1}) in a 1 M and 0.1 M $HClO_4$ matrix. The carbon CEs were burned in a muffle furnace at 600 °C for 10 h inside of quartz glass beakers (VWR, 50 ml). After burning the samples, no carbon residues were identifiable in the beakers by eye. To dissolve the remaining metal traces, 20 ml of concentrated aqua regia (36 wt% HCl (Suprapur, Merck KGaA) and 65 wt% HNO_3 (Suprapur, Merck KGaA) in a 3:1 volumetric mixture) was added to the beakers. The liquid was brought to a boil until ~ 5 ml remained. Then, the liquid was transferred and filled up to 50 ml with DI water in volumetric flasks. To ensure complete transferal of the dissolved Ir, the quartz beakers were rinsed 3 times with ~ 10 ml of DI water, which was added to the volumetric flask. The cleaning of the glassware was conducted after each quantitative analysis by rinsing with concentrated aqua regia, boiling in 1 wt% HNO_3 and again rinsing multiple times with DI water.

IEC was utilized to determine the concentration of crossover ClO_4^- in the anodic water cycle. The instrument was calibrated by standard solutions containing a known ClO_4^- concentration (4 – 196 mg l^{-1} $NaClO_4$ in DI water).

To investigate the sputter-coated platinum layers, Pt was deposited on silicon substrates coated with SiO_2 and Si_3N_4 membrane transmission electron microscopy (TEM) grids by sputter coating. The coating was conducted together with the PTLs at the same conditions stated above. A Talos F200i (Thermo Fisher Scientific) was used for STEM imaging, equipped with a Dual Bruker XFlash 6 | 100 energy-dispersive X-ray spectrum (EDXS) detector and a Schottky field-emission gun (X-FEG). The beam current and primary electron energy were 41 pA and 200 keV, respectively, with a convergence angle of 10.5 mrad. A high-angle annular dark field detector (HAADF) was used to detect elastically scattered electrons in an angular range of 58 to 200 mrad. The thickness of the Pt layers was additionally determined via reflectance microspectroscopy, as described in detail elsewhere.[35–38] The spectra were recorded with a 10x/ NA 0.25 objective lens coupled to a Horiba iHR 320 spectrometer equipped with a 1200 g/mm diffraction grating and a Horiba Synapse CCD detector. The refractive indices for Air,[39] Si,[40] SiO_2,[41] and Pt (ref.[42] for ~ 5 nm film, ref.[43] for thicker films) were taken from literature.

Scanning electron microscopy (SEM)-EDXS was conducted on the interface between the Ti-PTL and the catalyst layers, after carefully peeling off the catalyst layer | membrane composite using an XFlash detector (Bruker) integrated into the SEM (Mira 3 Tescan) operated at a primary electron energy of 5 keV.

Furthermore, cross-sectional HAADF-STEM imaging was performed on FIB-prepared TEM lamellae. The standard lift-out procedure used a Ga^+ ion beam in a dual-beam SEM (LYRA Tescan) equipped with a gas injection system. Silicon oxide was deposited at the area of interest via electron beam-induced deposition, followed by ion beam-induced deposition. A two-step polishing process was applied, using an energy of 30 keV initially and 10 keV subsequently, to minimize the amorphization of the lamellae. The average thickness of the lamellae was below 100 nm.

3. Results

Throughout this study, the dependency of the activity and stability of PTEs based on amorphous IrO_x and rutile IrO_2/TiO_2 on the Pt coating of the PTL was determined via polarization curves and chronopotentiometry at 1 A cm^{-2}. The full electrochemical protocol can be found in Table S 1. To investigate the influence of the Pt layer thickness on the OER performance, commercially available Ti PTLs were sputter-coated with Pt until specific Pt loadings, determined by weighing the samples before and after sputtering, were obtained, see Table 1.

The used GDE half-cell setup is shown in Fig. 1A. Only the side of the PTE facing the Ir-oxide-based catalyst layers was coated with Pt, Fig. 1B. Pt was sputtered on the native oxide layer forming on the Ti PTL already at ambient conditions due to Ti's high reducing power. Additionally, the Pt was sputtered onto Si_3N_4 membrane TEM grids and silicon substrates

Table 1
Designation and corresponding Pt loadings for the in-house platinized PTLs.

Designation	Nominal loading / mg_{Pt} cm^{-2}	Determined loading/ mg_{Pt} cm^{-2}
No Pt	0	0
Low Pt	0.01	0.013 ± 0.002
Mid Pt	0.05	0.050 ± 0.003
High Pt	0.10	0.100 ± 0.0003
Highest Pt	0.15	0.171 ± 0.003

coated with SiO_2 to obtain the surface morphology and thickness of the Pt layers via HAADF-STEM imaging and reflectance microspectroscopy, Fig. 1C–J.

At the lowest investigated loading of 0.01 mg_{Pt} cm^{-2}, the layer already looks rather homogeneous (Fig. 1C). Higher magnifications, however, reveal that the film is not yet fully closed (Fig. 1G). At higher Pt loadings, the surface of the Pt layer becomes closed (Fig. 1D, E, F), with crystallites typically larger than 10 nm in diameter (Fig. 1H, I). The Pt layer thickness, as calculated from the density of Pt, agrees well with the thickness obtained from reflectance microspectroscopy, Fig. 1J. At a loading of 0.01 mg_{Pt} cm^{-2}, the total layer thickness is lower than the typical crystallite size, which might explain why a cracked surface is formed at this low loading. The HAADF-STEM images clearly indicate that the sputtering device can deposit homogeneous, polycrystalline Pt thin films on smooth surfaces.

After investigating the film quality of the platinized PTLs at different loadings, electrochemical measurements of the PTEs were conducted in the GDE setup. High-frequency resistance (HFR) corrected polarization curves, depicting the influence of the sputtered Pt layer on the OER performance of PTEs based on amorphous IrO_x and rutile IrO_2/TiO_2 are presented in Fig. 2.

For amorphous IrO_x, the observed overpotential decreases with increasing Pt loading, up to 0.1 mg_{Pt} cm^{-2}. A higher Pt layer thickness does not improve the observed OER performance further. Below a Pt loading of 0.1 mg_{Pt} cm^{-2}, strong deviations between the measured samples were observed, especially at the low investigated Pt loading. These deviations might originate from an inhomogeneous Pt surface at this low loading (cf. Fig. 1G). Since sputter coating does not coat the material conformally, more Pt will be deposited on the outermost surface of the PTL. Due to the curved and rough surface of the fiber sinter

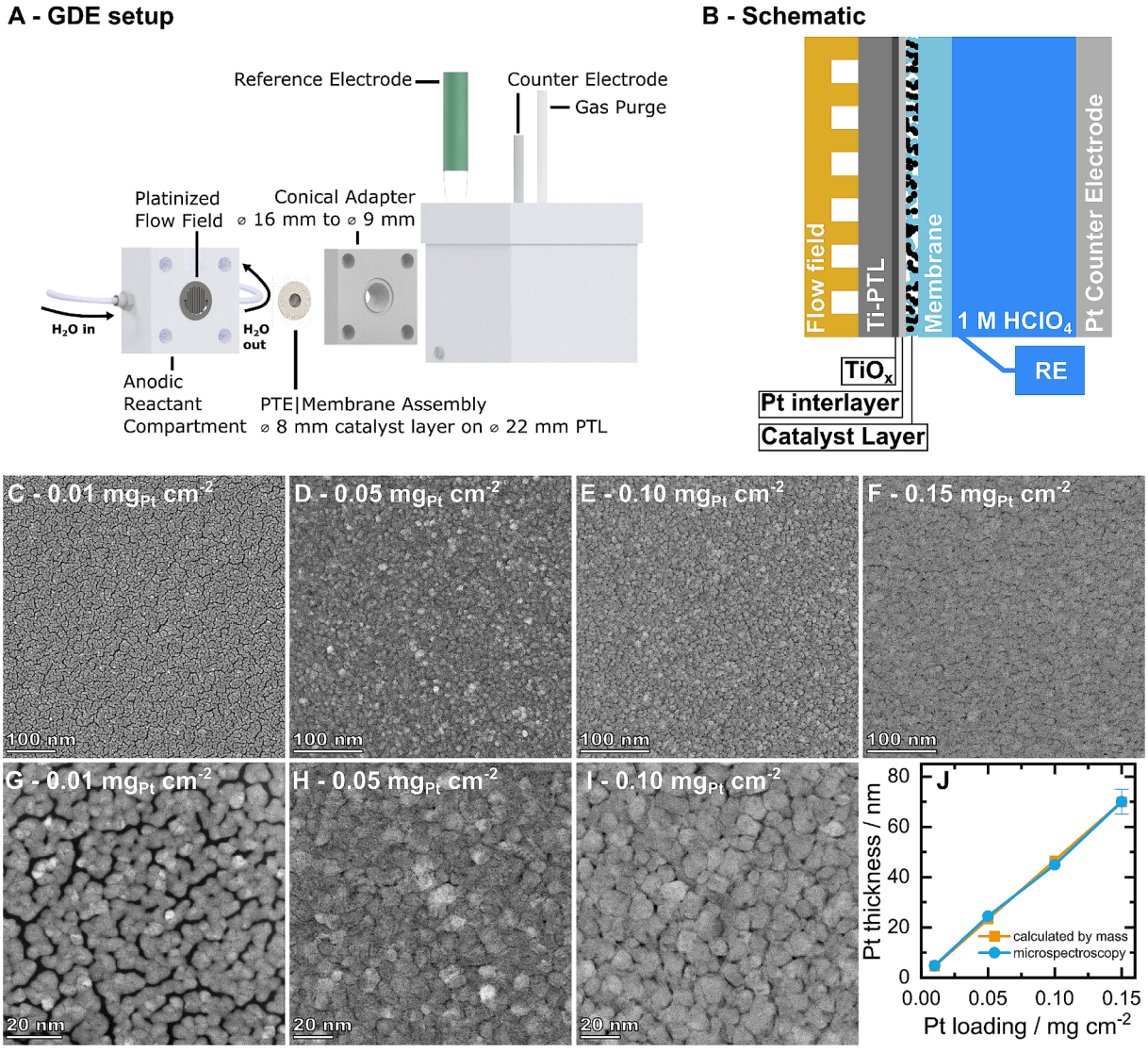

Fig. 1. A rendered image of the used GDE setup (A) and a schematic (B) showing the structure of the measurement device. The Pt interlayer was only sputtered onto the side of the PTL that was in contact with the spray-coated catalyst layer. The native Ti-oxide layer is shown for clarity. Top-view HAADF-STEM images of the sputtered Pt layers on Si_3N_4 membranes at different nominal loadings and magnifications (C – I) and Pt thickness determined via reflectance microspectroscopy and via the sputtered mass, assuming a Pt density of 21.45 g cm^{-3} (J).

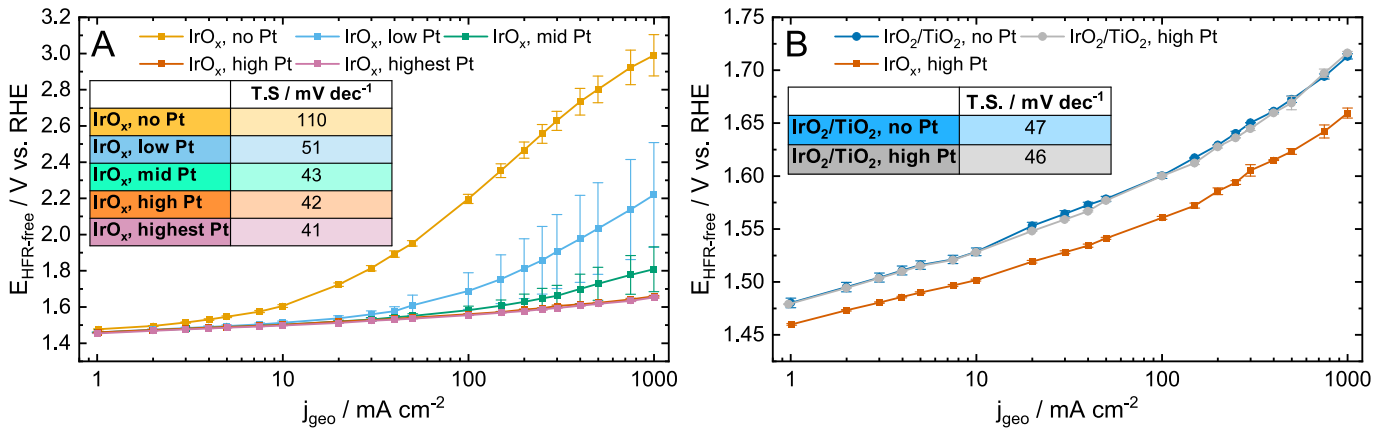

Fig. 2. HFR-free polarization curves recorded at 25 °C for amorphous IrO_x (A) and rutile IrO_2/TiO_2 (B) at constant Ir loadings (1 mg_{Ir} cm^{-2}) and varying Pt loadings. Tafel slopes (T.S.) were obtained between 1 and 10 mA cm^{-2}.

PTL,[44] the film thickness might not be as homogeneous as observed on the Si_3N_4 membranes coated for the TEM characterization. Protruding fibers might shade underlying parts of the PTL surface, largely preventing the coating of these underlying areas at low Pt loadings. Additionally, the deviation of the Pt loading between the low-loaded samples was ± 15 % (Table 1), with the observed overpotential being inversely proportional to the loading deviation, cf. Fig. S1. Thus, even small deviations at low Pt loading strongly influence the OER performance.

In contrast to amorphous IrO_x, for rutile IrO_2/TiO_2 (Fig. 2B), the overpotential is independent of the platinization degree. The overpotential is slightly higher than for amorphous IrO_x at high Pt loading, as expected from the literature.[10,24] The Tafel slopes, obtained between 1 and 10 mA cm^{-2}, were 46 – 47 mV dec^{-1} for rutile IrO_2/TiO_2 and 41 – 43 mV dec^{-1} for amorphous IrO_x from mid Pt loadings upward. Both values agree well with Tafel slopes reported for thermally prepared IrO_2 thin films[45] and amorphous IrO_x thin films.[46] At low Pt loadings, the Tafel slopes and the overpotential increase significantly for amorphous IrO_x, which we want to elucidate further by investigating the obtained impedance spectra, shown in Fig. 3.

For amorphous IrO_x, the shape of the Nyquist plots at open-circuit potential (OCP) changes significantly for different Pt loadings, which is visible in Fig. 3A. An arc resembling a parallel circuit of a capacitor and a resistor appears for no-Pt to mid-Pt loadings.[47] A similar arc was also observed in battery research when conducting electrochemical impedance spectroscopy around open circuit voltage.[48,49] This arc was attributed to a parallel circuit consisting of the current collector | electrode composite material contact resistance and the double layer capacitance of the current collector.[50] The diameter of the high-frequency arc decreased, while the frequency at the maxima of the arcs increased with increasing compression of the current collector and electrodes before the EIS measurements.[48] Hence, the similarly decreasing diameter and increasing frequency at the maxima of the investigated PTEs (Fig. 3A and B) might indicate a decreasing contact resistance between the CL based on amorphous IrO_x and the PTL, depending on the platinum interlayer thickness.

The frequency of the HFR intercept with the x-axis decreases with increasing Pt loading (table in Fig. 3A) for amorphous IrO_x. In contrast, for rutile IrO_2/TiO_2, independently of the Pt loading, the HFR intercept stays constant at ~ 3 – 10 kHz. For amorphous IrO_x at high Pt loading and rutile IrO_2/TiO_2 (Fig. 3B and C), the impedance resembles a constant phase element's capacitive behavior (no faradaic currents at OCP).[18,48] At high frequencies (~ 1 MHz – 100 kHz), an inductive feature appears, usually attributed to the self-inductance of the cell cables.[47] The inductive loop also changes slightly between experiments, which could be explained by artifacts related to the reference electrode and counter electrode compartment in three-electrode cells.[51,52] The

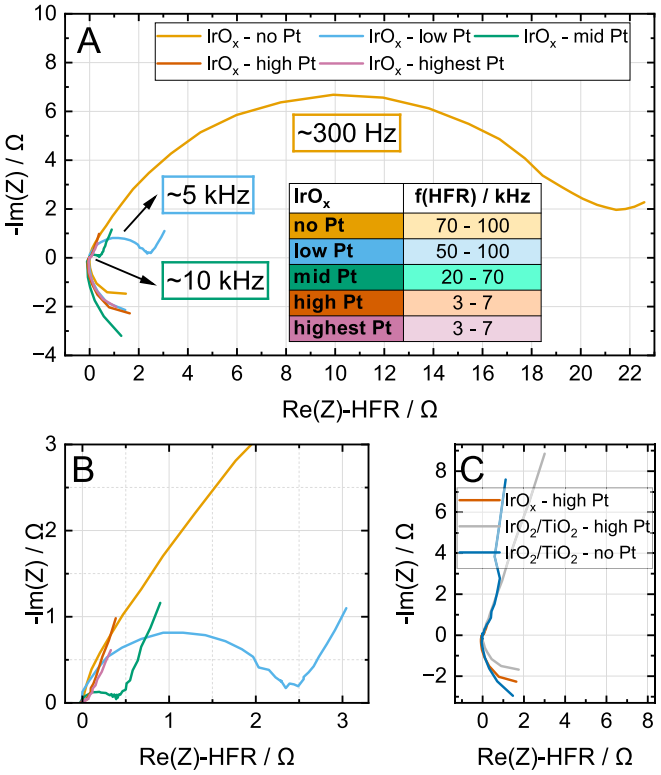

Fig. 3. HFR-subtracted Nyquist plots for amorphous IrO_x (A) and rutile IrO_2/TiO_2 (C) with different Pt loadings at OCP and enlarged area around the HFR (B). The colored boxes show the frequency maxima of the high-frequency arcs. The frequencies of the HFR in the end of the electrochemical protocol are given in the inset table. Spectra were recorded with an amplitude of 10 mV around OCP between 1 MHz and 1 Hz at 25 °C in the GDE half-cell setup.

system's high-frequency resistance was usually in the range of 5 Ω, which is in reasonable agreement with resistivity calculations for 1 M $HClO_4$.[53] Hence, we did not consider the influence of the cell cables' inductance or other artifacts for the impedance analysis conducted here.[54].

A low OER performance of CCMs prepared from amorphous IrO_x and operated without platinized PTLs was also reported in single-cell electrolyzers.[10,16,24,55] In contrast to the prepared PTEs measured in the GDE half-cell setup, the performances of the single-cell-tested CCMs only degraded for low loadings. At loadings of 0.50 mg_{Ir} cm^{-2}, decent performances were observed for the CCMs measured in single cells

($E_{HFR\text{-}free}$ 1.55 V at 1 A cm^{-2}),[55] while here poor performances were observed for PTEs with loadings of 1 mg_{Ir} cm^{-2} and higher, cf Fig. S2. This discrepancy could be related to the spray-coated PTEs forming inhomogeneous catalyst layers, reducing the amount of accessible active sites and, thus, the effective Ir loading.[44,56] Also, in single cells, a certain cell compression is applied during the measurements, which could reduce the contact resistance between the cell components, including the PTL | CL interfacial resistance. While the membrane in the GDE half-cell setup is hot-pressed onto the PTE during the preparation of the samples, throughout the measurement, the membrane is only in contact with the liquid electrolyte. Lacking the mechanical compression of the single cells might emphasize the contact resistance between PTL and CL. For single-cell measurements of these low-performing CCMs – consisting of low-loaded amorphous Ir-oxide in contact with non-platinized PTLs – to the best of our knowledge, only cell voltages, not HFR-free voltages, are presented.[10,16,24,55] The high-frequency arc observed here and in battery research, as discussed in the paragraph above, was also observed during the single cell measurements. In single cells, however, this arc starts appearing above the x-axis of the Nyquist plot at high frequencies (150—100 kHz), interfering with an accurate determination of the HFR, especially at higher current densities.[16] In the GDE half-cell setup, the HFR can be extracted from the intersection with the x-axis in the Nyquist plot, even without Pt coating at high current densities, Fig. 4.

The frequency of the HFR intercept at all current densities without Pt coating (Fig. 4A) and with low Pt loading (Fig. 4B) remains around 70 kHz and 50 kHz, respectively. The frequency maxima of the high-frequency arcs observed for these samples increases from low to high current densities, see boxed values in the Nyquist plots. A low-frequency arc was observed at intermediate current densities, e.g. at 100 mA cm^{-2} for low and high Pt loading (Fig. 4 B and C), with the frequency at the maximum around 5 Hz for amorphous IrO_x and around 32 Hz for rutile IrO_2/TiO_2 (Fig. S3). Due to its frequency range, we attribute this low-frequency arc to the OER charge transfer.[10,16]. Without Pt coating, the huge high-frequency arc overlaps significantly with this charge transfer arc, which, therefore, cannot be discerned unambiguously (Fig. 4A). Due to bubbles forming in the liquid electrolyte at higher current densities, the resistance fluctuates, and the impedance spectra become noisy, especially in the low-frequency region, where data

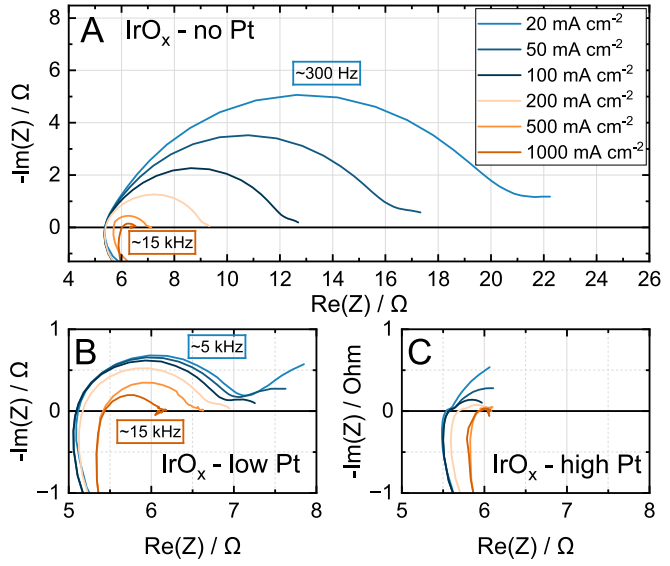

Fig. 4. Nyquist plots for amorphous IrO_x (A) without Pt interlayer, (B) with low loaded Pt interlayer and (C) with high loaded Pt interlayer at different current densities. The colored boxes show the frequency maxima of the high-frequency arcs. Spectra were recorded between 1 MHz and 1 Hz at 25 °C in the GDE half-cell setup.

acquisition takes longer. Hence, the low-frequency arc can no longer be observed at high current densities, e.g. at 1 A cm^{-2} for IrO_x with low Pt, Fig. 4B. The HFR obtained from the x-axis intercept increases for higher current densities, which we also ascribe to bubbles in the liquid electrolyte. These bubbles attach to the sides of the electrolyte container, increasing the measured resistance between the working and reference electrode. Upon detachment of the bubbles, the HFR decreases again.

Initially established for fuel cell diagnostics, transmission line modeling uses data obtained from electrochemical impedance spectroscopy to account for ohmic resistances in the cell while disregarding the resistance of the catalyst layers due to highly electrically conductive catalyst supports.[57] In the present study, the HFR should mainly account for ionic resistances in the liquid electrolyte (1 M $HClO_4$) and the membrane. Additionally, electronic bulk resistances of the flow field, the PTL, and cables, as well as contact resistances between the flow field and PTL, and the PTL and CL contribute. Recently, it was shown that the HFR also includes the charge transport resistance in the CL if its electronic resistance is non-negligible.[58] If the platinization of the PTL improved the contact resistance between the PTL and CL, the high-frequency intercept should shift to lower values for increasing platinization. In the used GDE half-cell setup, independently of the PTL's platinization degree, the high-frequency intercept of the Nyquist spectra was in the region of 5 – 6 Ω, without a clear trend in HFR, compare Fig. 4B and C. Therefore, (I) the difference in contact resistance is either too small to be perceived in the Nyquist plots obtained in the GDE half-cell setup, or (II) the contact resistance between PTL and CL is not purely ohmic, e.g. by the formation of a Schottky-like junction.[24].

To probe the influence of the CL|PTL interface on the stability of the PTEs, the dissolution of Ir was traced throughout a chronopotentiometric hold at 1 A cm^{-2}. The concentration of dissolved Ir in the anodic water cycle and the liquid electrolyte before and after the hold, as well as the redeposited Ir on the counter electrode, were determined. From the obtained concentrations and the passed charge, the S-number was calculated, as discussed in our previous publication.[30] The S-number is a metric for catalyst stability, normalizing the amount of O_2 evolved by the amount of Ir dissolved during the same time:

$$\text{S} - \text{number} = \frac{n(O_2)}{n(Ir)} \quad \text{(I)}$$

Fig. 5A shows the S-numbers for PTEs based on amorphous IrO_x and rutile IrO_2/TiO_2 at different platinization levels.

For amorphous IrO_x and rutile IrO_2/TiO_2, the observed S-numbers are independent of the Pt layer thickness. The S-numbers for rutile IrO_2/TiO_2 are more than an order of magnitude larger than for amorphous IrO_x. While the S-numbers remain similar, the HFR-corrected potential for PTEs based on amorphous IrO_x strongly depends on the platinization of the PTL (Fig. 2A). This indicates that either the stability of amorphous IrO_x during the OER depends more on the passed charge than on the applied potential, or the HFR-free potential does not represent the real potential at the active surface. Isotope labeling experiments indicate the participation of lattice oxygen during the OER, increasing the dissolution by a change in the reaction mechanism,[59] which suggests a close relation between the OER and Ir dissolution. At the end of the electrochemical protocol, less than 1.5 wt% and less than 0.1 wt% of the total amorphous and rutile Ir-oxide on the electrode dissolved, respectively. Assuming an OER Tafel slope of 50 mV dec^{-1} and a reduction of the electrode loading by 2 % from 1 mg_{Ir} cm^{-2} to 0.98 mg_{Ir} cm^{-2}, at 1 A cm^{-2}, this decrease in Ir loading should only lead to an increase in overpotential by less than 1 mV. Following Tafel kinetics, the increase in the overpotential due to the decreasing Ir loading is negligible compared to the observed differences in overpotential at different Pt loadings on the PTL. Regarding the HFR-free potential, the high-frequency arc observed for the low-platinized PTEs based on amorphous IrO_x (Fig. 3A) was ascribed to the interface resistance between the PTL and the CL,[24] Fig. 5C. Even including this interface resistance – additionally to the HFR – to correct for the potential drop, the potentials at the anodic

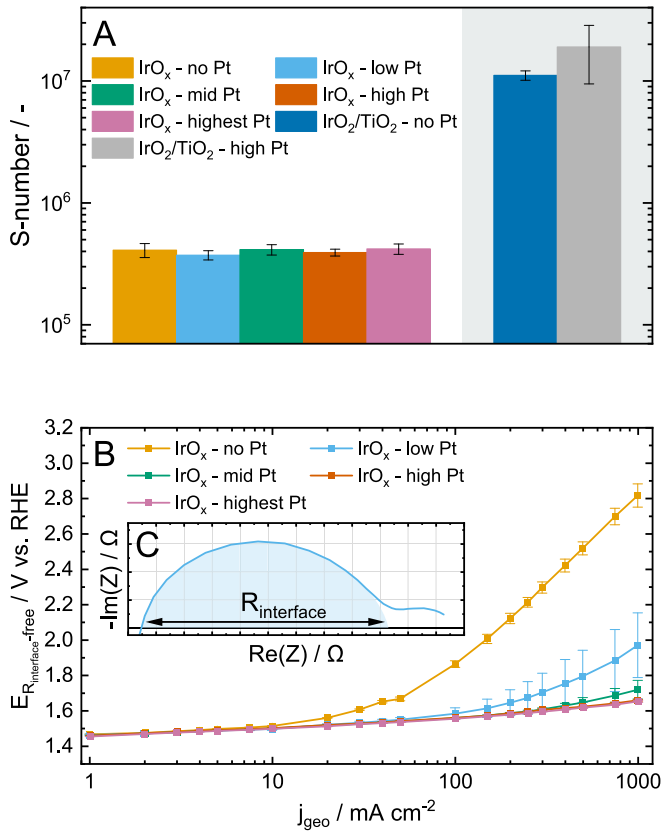

Fig. 5. (A) S-numbers recorded for PTEs based on amorphous IrO_x and rutile IrO_2/TiO_2 and different platinization degrees of the PTL. Chronopotentiometric holds were conducted for 20 min at 1 A cm^{-2} for all samples. (B) $R_{interface}$-corrected polarization curves, including the presumed interface resistance between the PTL and CL, obtained from the high-frequency arc as illustrated in (C). All electrochemical measurements were conducted in the GDE half-cell setup at 25 °C.

catalyst layer without platinization remain high, as seen in Fig. 5B. This is because the high-frequency arc reduces with increasing OER overpotential, Fig. 4, which we discuss in the following.

4. Discussion

The platinization of the PTL strongly influences the observed OER performance (Fig. 2A) and the shape of the Nyquist plots (Figs. 3 and 4) for PTEs based on amorphous IrO_x. Pt was shown to have a lower OER activity than Ir in aqueous model systems,[60] and we observed no increase in the OER activity of PTEs based on rutile IrO_2/TiO_2 with increasing platinization, Fig. 2B. Therefore, we assume the Pt interlayer has no significant catalytic effect on the prepared PTEs. The high-frequency arc was only observed for lower Pt loadings (Fig. 4), and its frequency range is higher than usually assumed for the OER charge transfer.[10,16] Hence, we attribute this arc to an equivalent circuit consisting of a parallel connection of a resistor and constant phase element, representing the CL|PTL interface. With increasing OER currents, and thus overpotential, the diameter of the high-frequency arc decreases. Doo *et al.*[24] attributed this observed high-frequency arc to the formation of a Schottky-type contact resistance between amorphous IrO_x (regarded as the high-work-function metal at the Schottky-type interface) and the native TiO_x formed on a non-platinized PTL (regarded as a low-work-function n-type semiconductor at the Schottky-type interface) in combination with the pinch-off effect. Upon formation of the interface, electrons move from the semiconductor to the available lower energy states in the metal. This movement of electrons from the conduction band leaves an electron-depleted region with high resistance in the semiconductor close to the metal interface. Rutile IrO_2 was shown to have a lower work function and was therefore considered to form an ohmic contact with TiO_x instead. During the OER, the electric potential in the PTL is higher than in the catalyst layer.[61] Hence, if an ideal Schottky-type junction formed at the CL|PTL interface, the junction would be backward biased during the OER, typically allowing only minor current densities by thermionic emission and tunneling.[62] Doo *et al.*[24] observed low OER performance only for very low-loaded IrO_x CCMs without platinized PTLs. They showed that the ionomer and membrane are in intimate contact with the PTL for very thin catalyst layers and claimed this induces the so-called pinch-off effect due to the mixed contact between TiO_x and IrO_x, and TiO_x and Nafion.

While the direct contact between the Ti-PTL and the metallic catalyst can result in the formation of Schottky junctions, the direct contact between the Ti-PTL and the ionomer binder might additionally induce this pinch-off effect.[63,64] The contact between an n-type semiconductor and an electrolyte will lead to band bending at the interface, similar to the contact between the semiconductor and a metal.[65] On a microscopic scale, the TiO_2 layer on top of the PTL is in direct contact either with the Ir-oxide or the ionomer binder in the catalyst layer. If a mixed contact between a semiconductor (TiO_2 layer on the Ti-PTL), a metal (Ir-oxide), and an electrolyte (Nafion) exists, the contact domain size between the phases can then influence the Schottky barrier height. The barrier height between the semiconductor and the metal will be influenced by the higher barrier (between the semiconductor and the metal or between the semiconductor and the electrolyte) if the contact domain size between the semiconductor and the metal decreases below a certain critical diameter. This threshold depends partially on the depletion width *W* in the semiconductor.

In the case of Doo *et al.*,[24] this higher barrier was assumed to be determined by the band-bending of the TiO_x in contact with the ionomer from the membrane and the catalyst layer. Mei *et al.*[66] showed this pinch-off effect for Pt nanoparticles and μm-size Pt islands on TiO_2-protected photoanodes, where no OER current was observed for the pinched-off Pt nanoparticles due to the formation of a Schottky-type contact. The rectifying Schottky contact between Pt nanoparticles and TiO_2 apparently prevented the flow of electrons from Pt to TiO_2. It was additionally shown that defect-free sputter-coated Pt-TiO_2 interfaces, where the TiO_2 is not in direct contact with the liquid electrolyte, form an ohmic-type contact.[66,67] Hence, the observed absence of OER activity for the Pt nanoparticles was attributed to the small domain diameter of the Pt-TiO_2 contact, leading to a pinch-off by the band-bending of the TiO_2 in contact with the liquid electrolyte.[66].

A decrease in the diameter of this high-frequency arc with increasing forward bias voltage was observed similarly for solar cells.[68,69] At increasing applied forward voltage, the barrier height at rectifying junctions decreases, reducing the resistance at the interface and thus the observed high-frequency arc. Therefore, in analogy to the decrease of the high-frequency arc for solar cells, the observed decrease of the high-frequency arc might indicate a facilitated transport of electrons from the IrO_x to the PTL at increased OER overpotential. The observed significant oxygen evolution currents for amorphous IrO_x in contact with the non-platinized PTL (Fig. 2A) point toward the interfacial contact not constituting a perfect Schottky contact since the rectifying property of a Schottky-junction should only allow small reverse currents.[62] During the OER, electrons would be moving against the rectifying direction of this Schottky-type contact. While the Ti PTL might theoretically be active for the OER, current densities of only 1 mA cm^{-2} were observed at potentials around 2.0 V vs. RHE for pure Ti-PTLs, see Fig. S4. Since oxygen evolution currents of 50 mA cm^{-2} were observed below 2 V vs. RHE for the non-platinized PTLs, we exclude a significant contribution of the Ti PTL to the measured OER currents. Additionally, during cyclic voltammetry, oxidative currents of more than 25 mA cm^{-2} were measured for amorphous IrO_x and the non-platinized PTL, Fig. 6A.

If a rectifying Schottky contact formed at the CL|PTL interface, the

anodic current densities during the CVs should be close to zero, as observed for ferri/ferrocyanide solution measurements.[66,70] At 1 V vs. RHE, the measured current was more than 4 times higher for amorphous IrO_x than for rutile IrO_2/TiO_2 without platinization, and the current densities increased with increasing IrO_x loading (Fig. S2B). The CVs of the samples with amorphous IrO_x and non-platinized PTLs appear distorted in comparison to the platinized PTL samples, which we attribute to an additional resistance that is not accounted for by the online HFR compensation. Additionally, CVs of the bare Ti-PTL (with membrane hot-pressed on top) exhibit current densities below 1 mA cm^{-2} in the investigated potential range, Fig. 6B. Hence, we can exclude that the observed CVs originate from double-layer charging of the PTL, which should otherwise also be observable for rutile IrO_2/TiO_2. On a side note, for rutile IrO_2/TiO_2, the electrochemical response of Pt during the CVs can be observed in Fig. 6B. Pt-oxide formation and reduction, as well as a distorted H_{UPD} region, can be observed from increased current densities for high platinization of the PTL, showing that the PTL|CL interface is ionically connected to the membrane via the ionomer and possibly due to the observed ClO_4^- crossover (Fig. S5).[30,34] For amorphous IrO_x, Pt's influence cannot be readily discerned due to pseudocapacitive charging and the transition of Ir^{III} to Ir^{IV},[71] inducing one order of magnitude higher current densities than for rutile IrO_2/TiO_2.

Both the OER currents and CVs indicate that electrons must pass the interface from the CL to the PTL, supporting an ohmic-type instead of a Schottky-type rectifying interfacial contact. In contrast, the appearance of a potential dependent high-frequency arc in the Nyquist plots supports a Schottky-type junction at low Pt loadings between the PTL and the CL, as discussed above. Since the pinch-off effect depends on the diameter of the contact area between semiconductor and metal,[63] we hypothesize that during the PTE preparation, a variety of individual contact domains between the amorphous IrO_x in the CL and the non-platinized PTL is formed. Some of these contact areas might be large enough not to be influenced by the pinch-off effect, in line with the varying structural size of PTEs prepared from the investigated IrO_x and IrO_2/TiO_2 catalysts observed from SEM imaging.[72] Hence, these contact areas would maintain ohmic characteristics and allow the flow of electrons through the CL | PTL interface during the OER, see schematic in Fig. 7A. At the same time, parts of the CL might be insulated during the OER due to the Schottky contact's rectifying property. Taking the charge of the CVs between 0.4 and 1.3 V vs. RHE as a relative measure of the available active sites,[73] without platinization, the number of available sites is reduced compared to the usage of platinized PTLs (Fig. 6A). Similar to the observed decrease in overpotential with increasing platinization (Fig. 2A), Chung *et al.*[27] observed a decrease in hydrogen evolution reaction (HER) overpotential of more than 100 mV at 10 mA cm^{-2} for poorly conductive MoS_2 when adding a conductive carbon support. They attributed the improvement to an improved contact between the backing electrode and the catalyst layer and increased electronic conductivity in the catalyst layer. With higher conductivity, the catalyst utilization and the effective overpotential at individual catalyst particles increase, improving the performance. Since

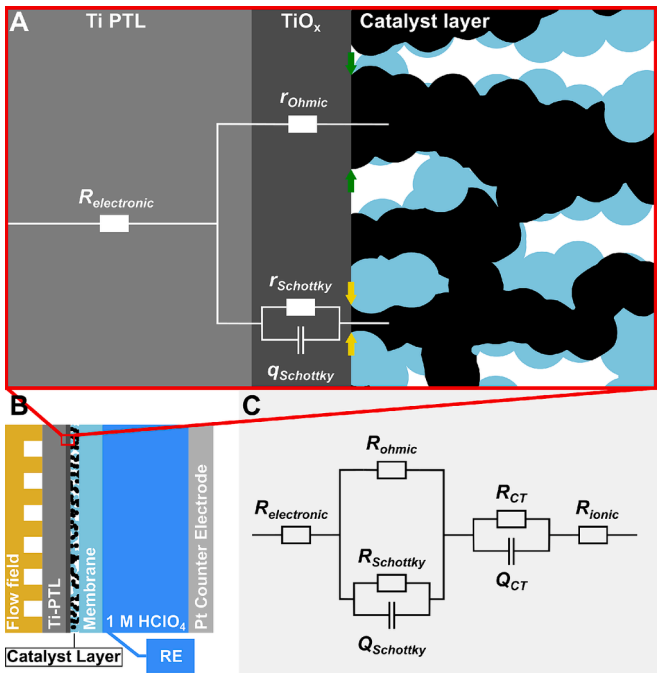

Fig. 7. (A) The PTL | CL interface schematic highlights the ohmic- and Schottky-type contacts at bigger (green arrows) and smaller catalyst contact domains (yellow arrows), respectively (Black: IrO_x; Blue: Ionomer). Schottky-type contacts are illustrated by double-layer elements ($q_{Schottky}$), representing charge accumulation at the interface, in parallel with the resistance $r_{Schottky}$ representing the Schottky-barrier height. Ohmic-type contacts are represented by r_{Ohmic}. (B) Schematic of the GDE half-cell setup (without Pt interlayer) to emphasize which part is shown in (A). (C) A simplified equivalent circuit representation of the GDE half-cell setup. $R_{electronic}$ is the sum of electronic bulk resistances of the flow field, the PTL, and the cables, as well as the contact resistance between the flow field and PTL. R_{ionic} represents the proton conduction resistance of the membrane and the liquid electrolyte. The catalyst layer is represented by a pseudo capacitance/double-layer element (Q_{CT}) parallel to the charge-transfer resistance (R_{CT}) representing the OER. The interface between PTL and CL is represented by the Schottky-type contact, consisting of $Q_{Schottky}$ ($= \Sigma\ q_{Schottky}$) in parallel with $R_{Schottky}$ ($1/R_{Schottky} = \Sigma\ (1/r_{Schottky})$), in parallel to the ohmic-type resistance R_{ohmic} ($1/R_{Ohmic} = \Sigma\ (1/r_{Ohmic})$).

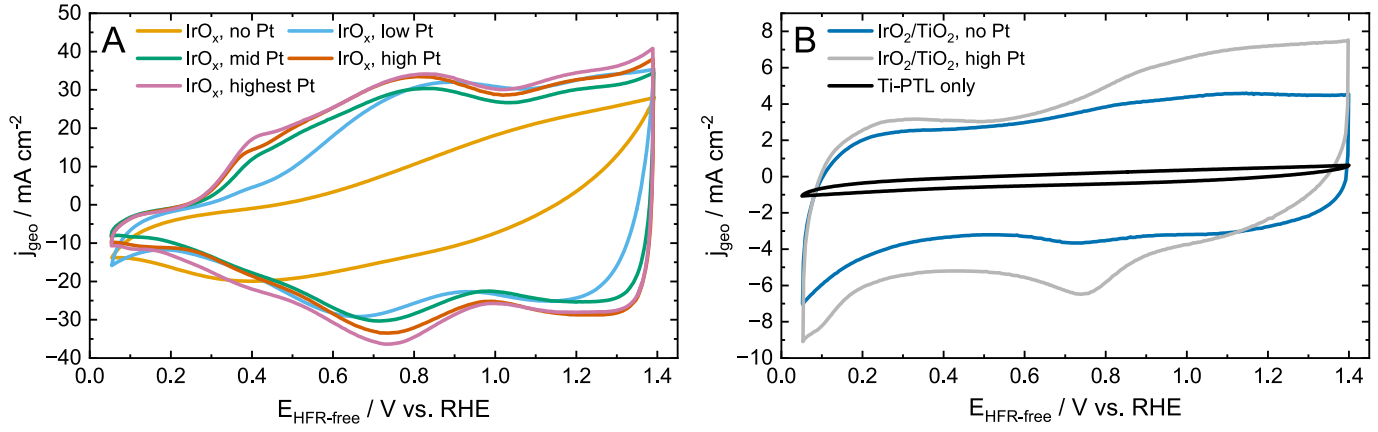

Fig. 6. Cyclic voltammograms (CVs) of the investigated (A) amorphous IrO_x-based PTEs and (B) rutile IrO_2/TiO_2-based PTEs with varying platinization degrees of the PTLs, as well as bare Ti-PTLs. CVs were conducted at 50 mV s^{-1} at 25 °C in the GDE half-cell setup.

the HFR was only determined at non-catalytically active potentials (0 V vs. RHE), they hypothesized that they could not observe the high electronic resistance of the catalyst layer in the HFR, which they observed from *ex situ* measurements. Analogously, a simplified equivalent circuit representation of the parallel ohmic- and Schottky-type contact, which can be expressed as a capacitor in parallel with a resistor,[74] can explain why the HFR might not include the contact resistance between PTL and CL, Fig. 7C.

Considering only the interface between PTL and CL, the interfacial impedance $Z_{interface}$ of two resistors and one double layer element in parallel can be expressed by:

$$Z_{Interface} = \frac{1}{1/R_{ohmic} + 1/R_{Schottky} + i\omega C_{CA}} \quad \text{(II)}$$

The term includes the resistance at ohmic-type domains R_{ohmic}, the resistance at the Schottky-type domains due to the barrier height $R_{Schottky}$, the radial frequency ω, the imaginary number i, and the charge accumulation capacitance C_{CA}. At very low frequencies, the capacitor acts as an open circuit and the ohmic resistance at the interface can be obtained:

$$Z_{Interface}(\omega \to 0) = R_{Interface} = \frac{R_{ohmic} \bullet R_{Schottky}}{R_{ohmic} + R_{Schottky}} \quad \text{(III)}$$

We assume the resistance at the Schottky-type domains is much higher than at the ohmic-type domains since the flow of electrons during the OER is suppressed at these domains due to the rectifying behavior of the Schottky barrier. As the smaller resistor governs the resistance of two resistors in parallel, $R_{interface}$ as obtained from the high-frequency arc in the Nyquist plots (Fig. 5C) would essentially correspond to the resistance of the ohmic-type domains R_{ohmic}. Since this $R_{interface}$ obtained from electrochemical impedance spectroscopy shows a dependence on the present potential (Fig. 4A, B), it also cannot be considered purely ohmic. Hence, from the presented model, the ohmic-type contact domains seem to partially constitute Schottky-type behavior while allowing the flow of electrons from the IrO_x to the TiO_x. This could be due to, e.g., the very thin Schottky barriers of these domains and impurities at the interface between PTL and CL, e.g., allowing tunneling of electrons, or Fermi-level pinning and high reverse currents.[64,66,75] TEM analysis[24] of the native TiO_x layer on a Ti PTL revealed a ~ 14 nm thick oxide layer, where only at the outermost surface the stoichiometry of the oxide

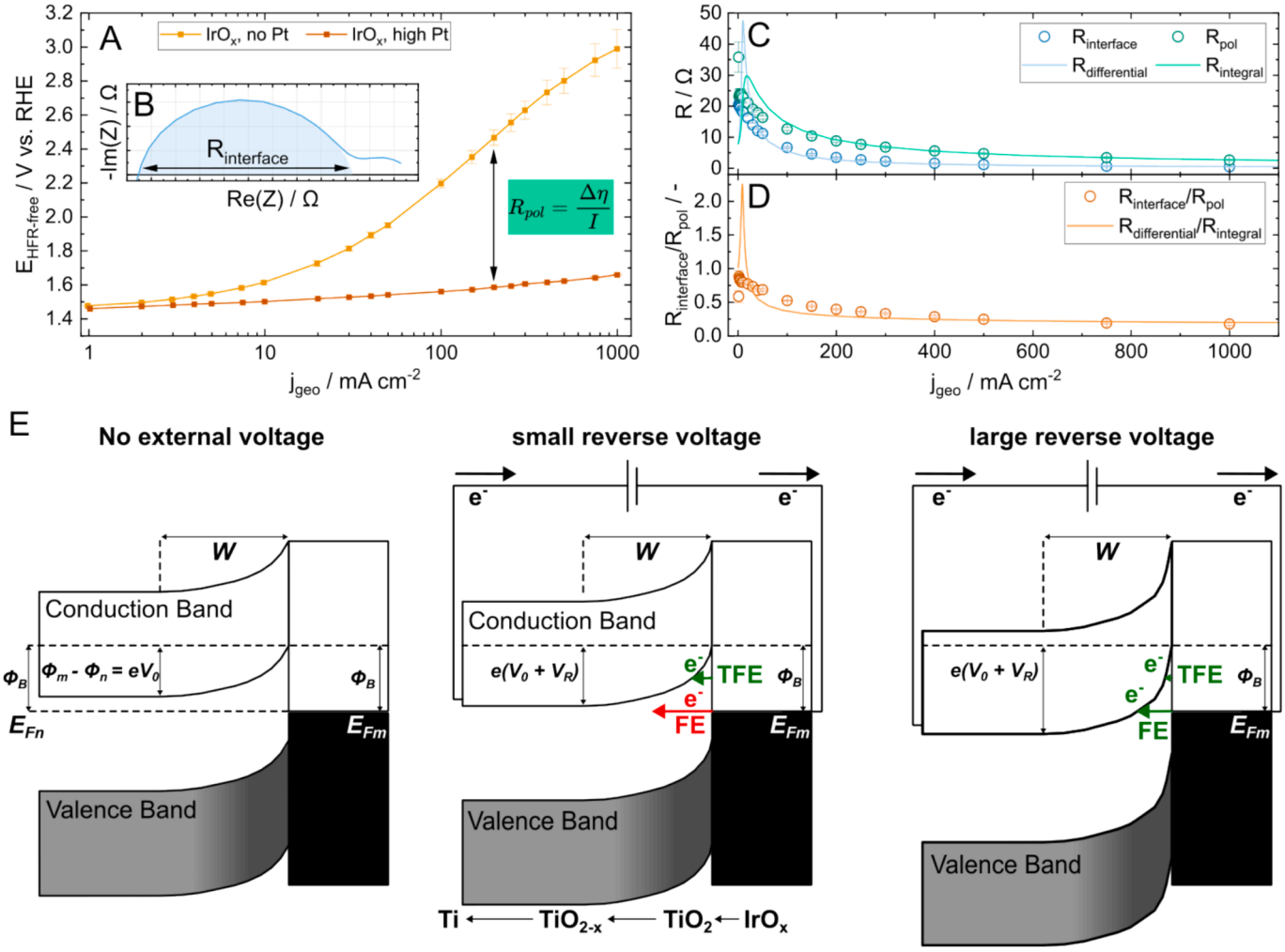

Fig. 8. (A) Polarization curves for amorphous IrO_x with and without platinization, with the determination of R_{pol} for fixed current densities. The inset (B) illustrates the interfacial resistance obtained from the Nyquist spectra. The experimentally determined resistance values are marked in (C), while the lines show the obtained resistances from the modeled diode equation. The ratio between integral and differential resistances (D) was obtained from experimental data (markers) and the modeled diode equation (lines). (E) A simplified schematic of a Schottky interface between the IrO_x catalyst and the TiO_x layer on top of the Ti-PTL during different applied external voltage. When no external voltage is applied, the Fermi level of the n-type semiconductor E_{Fn} and the metal E_{Fm} align. A depletion region of width W and barrier height Φ_B forms in the semiconductor at the interface. The difference in the work function of the metal Φ_m and the semiconductor Φ_n leads to forming the so-called built-in potential V_0. The application of an external reverse voltage V_R effectively shifts the semiconductor band diagram downward regarding the metal side. Field emission *FE* and thermionic field emission *TFE* are shown as main conducting mechanisms for very thin depletion regions.

resembles TiO_2 (~ 1 nm thick) and then decreases towards oxygen-deficient TiO_{2-x}. The conductivity of TiO_2 was shown to increase by orders of magnitude already at very low amounts of oxygen vacancies.[76] Since the semi-conducting TiO_x layer is very thin and its conductivity should increase strongly below the surface, we hypothesize that the charge depletion region and the Schottky barrier width are relatively small. Assuming that the electrons flow through the contact domains with the lowest barrier heights,[66] parts of the CL would be insulated and inactive. Then, similar to the model proposed by Chung *et al.*,[27] the catalyst utilization would decrease, and the OER performance decreases with decreasing platinization.

To further examine if the observed semicircle in the Nyquist spectra can be correlated to the observed increase in overpotential, a comparison between amorphous IrO_x with and without Pt coating was conducted. The additional overpotential $\Delta\eta$ at a constant current density without platinization can be used to determine an integral resistance R_{pol} via Ohm's law, Fig. 8A. The interfacial resistance $R_{interface}$ obtained from the high-frequency arc should be differential, since it is obtained from impedance spectroscopy (Fig. 8B). Due to the small ac perturbations during impedance spectroscopy, the impedance can be approximated by the differential $d\eta/di$. The obtained resistances $R_{interface}$ and R_{pol} decrease with increasing current density (Fig. 8C), while R_{pol} is generally higher than $R_{interface}$ (Fig. 8D).

Assuming a thin depletion region at the Schottky interface due to the thin TiO_2 layer on top of the PTL, thermionic field emission (TFE) and field-emission (FE) tunneling might become the dominating electron transport mechanisms, allowing higher reverse currents across the Schottky interface.[77,78] The reverse current–voltage characteristics across the interface can be approximated by an exponential diode equation:[77,79]

$$j_{Schottky} = j_R \left[e^{\left(1-\frac{1}{n}\right)\frac{q}{kT}\Delta\eta} - e^{-\frac{q}{nkT}\Delta\eta} \right] \quad \text{(IV)}$$

The pre-exponential factor j_R depends inter alia on the temperature, the Richardson coefficient of the semiconductor and the Schottky barrier height. Additionally, the equation contains the elementary charge q, the Boltzmann constant k, and the temperature T. The ideality factor n describes the deviation of the real Schottky interface from an ideal interface. For $n = 1$, the reverse current at the interface approaches j_R under moderate reverse bias, and the equation simplifies to the ideal diode equation. For $n = 2$, forward and reverse j-V characteristics at the interface are equal. Hence, this corresponds to electrons flowing equally facile in both directions through the Schottky interface. The reverse voltage across the Schottky interface V_R can be approximated by the additional overpotential $\Delta\eta$ to fit this exponential diode equation to the electrochemical data for amorphous IrO_x without platinization. Subsequently, the integral and differential resistance can be obtained from Ohm's law and the derivative of the equation, respectively. The calculations for Eq. (IV) and for the Butler-Volmer equation, with different fitting parameters, are described in the Supporting information section 7. This simple approach already yields an acceptable agreement with the experimentally obtained resistances and the ratio between the resistances obtained from the polarization curves and the Nyquist plots, see lines in Fig. 8C and D. At low current densities (< 20 mA cm^{-2}), $R_{differential}$ and $R_{integral}$ exhibit a peak, whereas R_{pol} and $R_{interface}$ show plateauing values. This difference between the experimentally determined resistance values and the values obtained from the fitted functions is still under investigation and might be due to, e.g., the complex interface between the catalyst layer and the PTL, as indicated in Fig. 7A, leading to different electron-conduction mechanisms. At low $\Delta\eta$, FE might be hindered by insufficient shifting of the semiconductor band diagram, as shown for low reverse voltage in Fig. 8E. Hence, at low current densities, other charge transport mechanisms like thermionic emission across the lowest barriers of the heterogeneous interface might dominate. Additionally, $\Delta\eta$ might not represent the reverse voltage V_R perfectly, leading to deviations between the experimental data and the fitted function, especially at low currents and, thus, low overpotentials. Adapting the exponential diode equation slightly, e.g. assuming $n = 2$, $R_{differential}$ and $R_{integral}$ decrease monotonously with increasing current density, similarly to R_{pol} and $R_{interface}$, see Supporting information section 7. Hence, in general, the decrease of R_{pol} and $R_{interface}$ with increasing current density and the ratio of both values further support the hypothesis that the observed high-frequency arc and the increase in overpotential are related to the same phenomena, probably by some additional interfacial resistance.

Since crystalline materials are generally considered harder and less elastic than amorphous materials,[80] it stands to reason that rutile IrO_2 is harder and less elastic than amorphous IrO_x. Additionally, Nafion was shown to bind stronger to hydrous IrOOH than to rutile IrO_2,[81] which might lead to an increased coverage of the hydrous Ir-oxide species by the ionomer. The PTEs based on amorphous and rutile Ir-oxides were prepared from identical ink compositions (except the active catalyst) and by the same spray-coating procedure, leading to comparable PTE morphologies as observed from cross-section SEM images for both oxides.[72] Nonetheless, the different interactions of hydrous and rutile Ir-oxide with the ionomer might lead to different distributions of the ionomer and the active catalyst in the catalyst layers and, hence, differences at the interface between PTL, catalyst, and ionomer. Inelastic rutile IrO_2 might pierce ionomer patches during the hot-pressing and cell assembly, whereas amorphous IrO_x might get compressed and rather be buried under the ionomer. Detailed imaging of the ionomer distribution inside the catalyst layer remains highly challenging[82] and is beyond the scope of the presented work. Still, to gain further insights into the interface between the catalyst layer and PTL, HAADF-STEM images of TEM lamellae from the interface between the PTL and the different catalysts, as well as the corresponding STEM-EDXS images are shown in Fig. 9 A-H.

The cross-section STEM-EDX spectrum images indicate a thicker oxide layer for the tested samples that contained amorphous IrO_x without a Pt layer on top of the Ti PTL compared to the samples that contained rutile IrO_2, or amorphous IrO_x in combination with the Pt layer on the Ti PTL, as also observed from the oxygen line profile (Fig. 9J). Additional elemental mapping of Ir and Ti is shown in Fig. S12. SEM-EDX spectra obtained from the top of the PTL | catalyst layer interface after peeling the catalyst layer off show a higher oxygen content for Ti-PTLs in direct contact with amorphous IrO_x, Fig. 9K. The top-view spectra were recorded at 4 keV to ensure a higher surface sensitivity while still detecting the Ir signal, thus allowing confirmation of the absence of the Ir-oxide-containing catalyst layer, which would otherwise contribute to the measured oxygen signal, see Fig. S13. These spectra indicate that the PTL surface of the tested amorphous IrO_x samples without platinization contain more oxygen than the rutile IrO_2 samples without platinization and the pristine PTLs before electrochemical testing, Fig. 9J. Also, the oxide layer on the amorphous IrO_x samples with platinized Ti-PTL appears thinner than without platinization, compare Fig. 9E and G. The results imply that the interface between amorphous IrO_x and the bare Ti-PTL oxidizes increasingly with electrochemical testing. A thicker oxide layer on the Ti-PTL could increase the Schottky barrier width between amorphous IrO_x and the Ti-PTL, furthering the observed lowered OER performance (Fig. 2).

Hence, in addition to differences in work function[24] and the pinch-off effect,[63] the differences in the TiO_x layer thickness might explain why amorphous IrO_x in direct contact with the Ti-PTL exhibits such a high overpotential for the OER. Inelastic rutile IrO_2 might contact the PTL more rigidly during sample preparation, avoiding the pinch-off effect by forming bigger contact domains on the Ti-PTL, as well as preventing excessive oxidation of the Ti-PTL during operation, forming an ohmic-like contact, as seen from impedance spectroscopy (Fig. 3C). In contrast, elastic amorphous IrO_x might compress during sample preparation, leading to smaller contact areas with the Ti-PTL and intimate

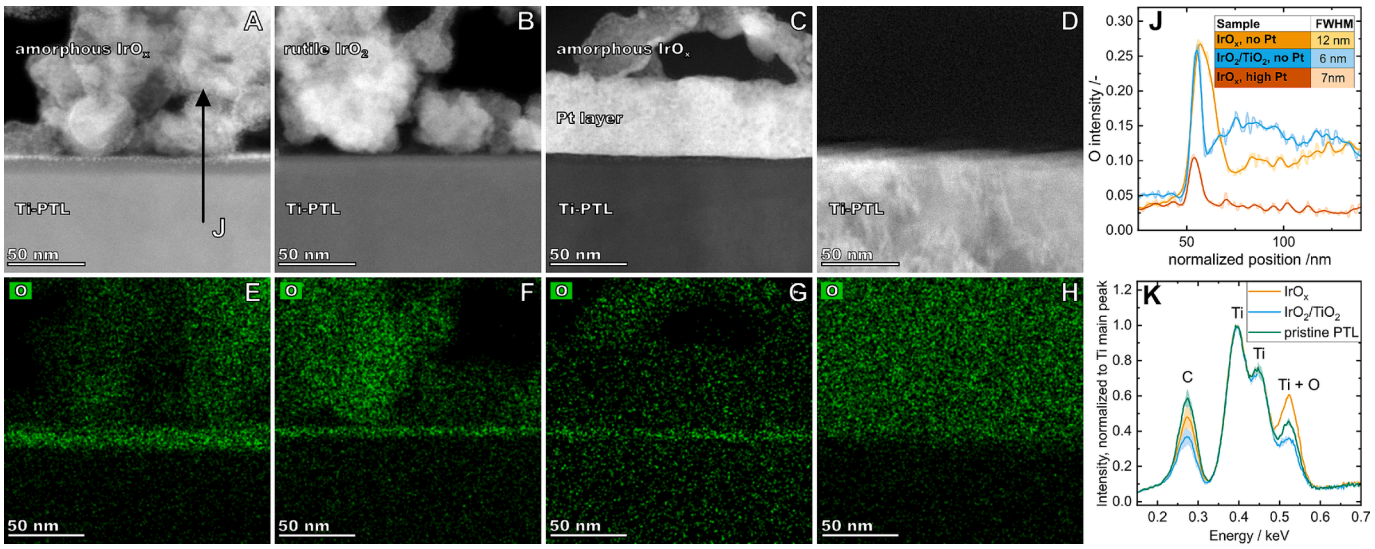

Fig. 9. Cross section HAADF-STEM images of the interface between the Ti-PTL and amorphous IrO_x (A), the Ti-PTL and rutile IrO_2 (B), the platinized PTL (high Pt) and amorphous IrO_x (C), and a pristine PTL (D), as well as the respective EDX spectrum image of the oxygen K_α signal (E-H). Oxygen line profile along the arrow (J) with the tabulated full width at half maximum (FWHM) for the oxygen peak corresponding to the Ti-oxide layer. SEM-EDX spectra (K) obtained from the top of the PTLs after removal of the catalyst layer, normalized to the Ti signal.

contact between the PTL and the ionomer, which can induce the pinch-off effect. Additionally, this seems to enhance the oxide layer at the PTL | catalyst layer interface. The growth of oxide thin films on metals can be described by Cabrera-Mott kinetics.[83] According to this approach, the growth rate of the oxide film depends on the voltage across the oxide thin film, which in turn depends on the adsorbed ions at the oxide | fluid interface. If the Ti-PTL is in intimate contact with Nafion in the case of elastic amorphous IrO_x, the double layer at the PTL | Nafion interface would be thin due to the high ionic strength of Nafion. This would lead to a high potential drop across the Ti-oxide layer and enhanced oxide growth, represented schematically in Fig. 10. During the preparation of the samples, the Nafion membrane was hot-pressed directly onto the PTE, which might increase the direct contact of the PTL with Nafion and enhance the pinch-off effect. This difference in the preparation could explain why the low performance of IrO_x-based PTEs is observed for high loadings in the GDE half-cell setup (Fig. S2) compared to single-cell studies.[24] Sputtered polycrystalline Pt, despite its high work function, was shown to form an ohmic-like contact with TiO_x (which also highlights the importance of the preparation method on the type of contact formed at interfaces).[66,84] Therefore, with increasing platinization, a closed Pt surface should form on the native TiO_x layer of the PTL, preventing direct contact with the ionomer and the pinch-off effect. This might enable good electronic contact between the PTL and the whole CL, improving the total OER activity (Fig. 2A).

Regarding the dissolution of Ir at different platinization degrees, Geiger *et al.*[25] observed similar Ir dissolution from Ir black on FTO and Au in an aqueous model system, even though the potential on FTO after 20 h of testing was ~ 500 mV higher. The increase in potential was ascribed to an increased contact resistance between FTO and Ir, compared to an Au backing electrode. Hence, it seems likely that in the present study, (I) either only small parts of the catalyst layer are active due to the rectifying properties of the Schottky-type contact, or (II) a significant part of the observed HFR-free overpotential acts as the driving force to overcome the Schottky-type barrier at the PTL | catalyst layer interface, or (III), due to inhomogeneous barrier heights throughout the PTL | catalyst layer interface, both mechanism (I) and (II) are active. Assuming explanation (III), the turnover frequency of the remaining active sites and the overpotential would increase due to the lower catalyst utilization and increasing mass- and charge-transport resistances. If the Ir dissolution were mainly driven by the OER,[85] lower utilization would not increase the S-number since the same total charge is passed, as seen in Fig. 5A. In single-cell electrolyzers with low-loaded IrO_x-based CCMs, the formation of an Ir band in the membrane – which indicates Ir dissolution – was found to be most pronounced in areas presumed to be most catalytically active.[18] No Ir band was observed for CL parts not directly in contact with the PTL and thus

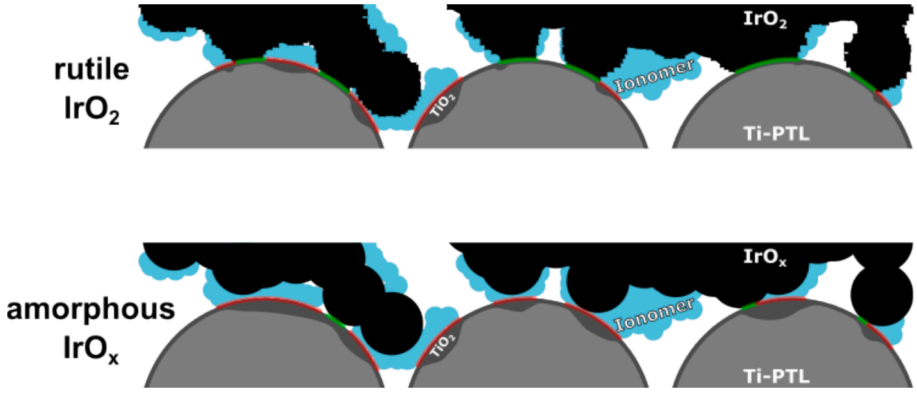

Fig. 10. The interface between the Ti-PTL, the rutile, the amorphous Ir-oxide, and the ionomer (blue). Dark grey indicates the native oxide layer on the Ti-PTL and increased oxidation by contact with the ionomer. Green and red indicate facile and inhibited electron transport across the catalyst layer | PTL interface, respectively.

presumed to be less active. If the dissolution of Ir is correlated to the passed oxygen evolution charge, then even though similar total dissolution was observed in the GDE half-cell setup for apparently different catalyst utilization, the lifetime in applied devices should depend on the uniformity and utilization of the catalyst layer. Electrochemically active parts of the CL would dissolve faster until contact between the CL and the PTL is lost, leading to inactivity of the whole catalyst layer. Generally, the interface between the PTL and the CL of a PEMWE anode is a very complex structure, which warrants further investigation to understand its properties but is beyond the scope of the current work.

5. Conclusion

This work presents unique insights into the influence of PTL-platinization on the performance and stability of Ir-oxide-based PTEs. Impedance analysis of the catalyst layers shows a semicircle formation in the Nyquist plots at high frequencies for amorphous IrO_x-based PTEs at low Pt interlayer thicknesses. Similar to the behavior observed for solar cells,[68,69] this semicircle decreases at higher current densities and, hence, higher OER overpotentials. We attributed this semicircle to the formation of a heterogeneous Schottky-type interface between the PTL and the catalyst layer. Since the flow of electrons during the OER would be opposite to the rectifying direction of the Schottky-type junction, high OER current densities would result in very high reverse current densities at the junction. This implies that the Schottky barrier heights should be very low to allow this flow of electrons, possibly due to a thin depletion width allowing charge transport by field emission and/or impurities at the CL|PTL interface and subsequential Fermi pinning in the semiconducting TiO_x layer. Assuming varying nanometer-sized contact domains between Ir-oxide and the PTL, different Schottky barrier heights might develop due to the pinch-off effect, and electrons would mainly traverse this interface at domains with the lowest barrier. To overcome this barrier, a certain reverse voltage needs to be applied to shift the semiconductor bands and allow increasing reverse currents. This reverse voltage would be added to the HFR-free potential of electrodes containing only ohmic interfaces. Additionally, parts of the catalyst layer might be insulated, leading to lower utilization and, thus, low OER performance of these catalyst layers.

Interestingly, the observed amount of dissolved Ir from the PTEs during chronopotentiometric holds was independent of the Pt interlayer thickness, even if it influenced the observed OER overpotentials heavily. Hence, either the Ir dissolution during the OER is closely intertwined with the reaction and less with the potential, or the correction of the measured cell voltage by the HFR and the effective potential at the active centers differ when a Schottky junction is present. Nonetheless, catalyst layers for applied electrolyzers might degrade faster for inhomogeneous utilization since increased punctual catalyst dissolution would increase catalyst layer resistances. During prolonged operation, the electrical contact between PTL and catalyst layer might be lost, deactivating the catalyst layer. For PTEs based on rutile IrO_2/TiO_2, no high-frequency arc was observed in the Nyquist plots, and the OER activity of these PTEs showed no dependency on the PTL-platinization. Amorphous IrO_x, shown as more active than rutile IrO_2 in AMS, only exhibits higher OER activity for the investigated PTEs with platinized PTLs.

The observed performance loss for catalyst layers based on amorphous IrO_x in contact with non-platinized Ti-PTLs was also observed in single-cell electrolyzers, albeit only at lower Ir-loadings ($< 0.50\ mg_{Ir}\ cm^{-2}$).[10,16,24,55] This discrepancy in loading dependency was attributed to the usage of PTEs in the GDE setup (in contrast to CCMs in single-cell electrolyzers) in combination with the direct membrane hot-pressing onto the catalyst layer and the usage of liquid electrolyte. Nonetheless, the presented results align with published data from single-cell electrolyzers and hence show that the GDE setup can further substantiate the understanding of charge-transport processes in application-relevant electrolyzer devices. The loading-dependent charge-transport-induced performance losses observed in single-cell electrolyzers can be overcome using different strategies. At higher, state-of-the-art Ir-loadings, amorphous IrO_x can be used as the OER catalyst since intimate contact between the Ti-PTL and the membrane is avoided by the thick catalyst layer, preventing the pinch-off effect.[24] At desired lower Ir-loadings, PGM interlayers between the Ti-PTL and the anode can prevent this direct contact between the Ti-PTL and the membrane and, thus, the formation of a charge-transport barrier.[16,22,55] Alternatively, catalysts with reduced Ir packing density[10,86] can be used to prepare thicker catalyst layers at low loadings, again preventing the pinch-off effect. Rutile, instead of amorphous Ir-oxide, can be used as the OER catalyst to avoid the formation of a Schottky junction and the associated voltage drop.[10,24] Additionally, microporous transport layers between the PTL and the anodic catalyst layer were shown to improve the performance of low-loaded anodes.[20,21] Besides the thorough preparation of the PTL | catalyst layer interface, cell voltage management throughout the electrolyzer operation might prevent excessive passivation of the Ti-PTL and an amorphization of the Ir-oxide[19] and hence avoid an increase in charge-transport barriers between these cell components. In conclusion, the obtained results indicate that for developing high-performing and stable electrodes for the OER in a half-cell setup, not solely the optimization of the catalyst layer and the PTL is important. Additionally, the interactions between the individual electrode parts can have a huge impact, which should also be considered for the transfer to single cells.

Authors contribution statement

Mo.G. and S.C. conceived and planned the experiments. Mo.G. carried out the experiments. Mo.G., L.L. manufactured electrodes. A.H. provided the TEM investigation. J.S. conducted the reflectance microspectroscopy. I.K. provided the SEM/EDX spectra. J.N. provided FIB lamellae. Mo.G., I.K., J.S., and A.H. analyzed and summarized the data. Mo.G., Mi.G., L.L., A.H., and S.C. contributed to the interpretation of the results. Mo.G. took the lead in writing the manuscript. All authors provided critical feedback and helped shape the research, analysis, and manuscript.

CRediT authorship contribution statement

Moritz Geuß: Writing – review & editing, Writing – original draft, Visualization, Software, Methodology, Investigation, Formal analysis, Data curation, Conceptualization. **Lukas Löttert:** Writing – review & editing, Methodology, Investigation. **Andreas Hutzler:** Writing – review & editing, Visualization, Methodology, Investigation, Formal analysis, Data curation. **Julian Schwarz:** Writing – review & editing, Methodology, Investigation. **Jaroslava Nováková:** Writing – review & editing, Methodology, Investigation. **Ivan Khalakhan:** Writing – review & editing, Visualization, Methodology, Investigation. **Miran Gaberšček:** Writing – review & editing, Methodology, Formal analysis, Conceptualization. **Karl J.J. Mayrhofer:** Writing – review & editing, Supervision, Funding acquisition. **Simon Thiele:** Writing – review & editing, Funding acquisition. **Serhiy Cherevko:** Writing – review & editing, Supervision, Resources, Methodology, Funding acquisition, Formal analysis, Conceptualization.

Declaration of competing interest

The authors declare no competing financial interest.

Acknowledgments

Mo.G., L.L., S.T., and S.C. gratefully acknowledge funding by the German Federal Ministry for Economic Affairs and Energy (BMWi) in the framework of HoKaWe (BMWi/03EI3029A). Mo.G. wants to thank Theresa Stigler for TGA measurements, as well as Christian Göllner for

all the support with ICP-MS and IEC measurements.

Appendix A. Supplementary data

Supplementary data to this article can be found online at https://doi.org/10.1016/j.cej.2025.162887.

Data availability

Data will be made available on request.

References

[1] Key developments in European electricity markets - 2024 Market Monitoring Report; European Union Agency for the Cooperation of Energy Regulators, 2024. https://www.acer.europa.eu/monitoring/MMR/electricity_key_developments_2024 (accessed 20 January 2025).

[2] M. Carmo, D.L. Fritz, J. Mergel, D. Stolten, A comprehensive review on PEM water electrolysis, Int. J. Hydrogen Energy 38 (2013) 4901–4934, https://doi.org/10.1016/j.ijhydene.2013.01.151.

[3] K. Ayers, N. Danilovic, R. Ouimet, M. Carmo, B. Pivovar, M. Bornstein, Perspectives on low-temperature electrolysis and potential for renewable hydrogen at scale, Annu. Rev. Chem. Biomol. Eng. 10 (2019) 219–239, https://doi.org/10.1146/annurev-chembioeng-060718-030241.

[4] L. Fiedler, T.-C. Ma, B. Fritsch, J.H. Risse, M. Lechner, D. Dworschak, M. Merklein, K.J.J. Mayrhofer, A. Hutzler, Stability of Bipolar Plate Materials for Proton-Exchange Membrane Water Electrolyzers: Dissolution of Titanium and Stainless Steel in DI Water and Highly Diluted Acid, ChemElectroChem 10 (2023) e202300373, https://doi.org/10.1002/celc.202300373.

[5] B.S. Pivovar, M.F. Ruth, D.J. Myers, H.N. Dinh, Hydrogen: Targeting $1/kg in 1 Decade, Electrochem. Soc. Interface 30 (2021) 61, https://doi.org/10.1149/2.F15214IF.

[6] A. Cowley, S. Brown, L. Cole, M. Fujita, N. Girardot, S. Grant., J. Jiang, R. Raithatha ,M. Ryan, B Tang, Johnson Matthey PGM Market Report, 2023.

[7] H. Yu, N. Danilovic, Y. Wang, W. Willis, A. Poozhikunnath, L. Bonville, C. Capuano, K. Ayers, R. Maric, Nano-size IrOx catalyst of high activity and stability in PEM water electrolyzer with ultra-low iridium loading, Appl. Catal., B 239 (2018) 133–146, https://doi.org/10.1016/j.apcatb.2018.07.064.

[8] Z. Taie, X. Peng, D. Kulkarni, I.V. Zenyuk, A.Z. Weber, C. Hagen, N. Danilovic, Pathway to Complete Energy Sector Decarbonization with Available Iridium Resources using Ultralow Loaded Water Electrolyzers, ACS Appl. Mater. Interfaces 12 (2020) 52701–52712, https://doi.org/10.1021/acsami.0c15687.

[9] J.K. Lee, G. Anderson, A.W. Tricker, F. Babbe, A. Madan, D.A. Cullen, J.D. Arregui-Mena, N. Danilovic, R. Mukundan, A.Z. Weber, X. Peng, Ionomer-free and recyclable porous-transport electrode for high-performing proton-exchange-membrane water electrolysis, Nat. Comm. 14 (2023) 4592, https://doi.org/10.1038/s41467-023-40375-x.

[10] M. Bernt, C. Schramm, J. Schröter, C. Gebauer, J. Byrknes, C. Eickes, H. A. Gasteiger, Effect of the IrOx Conductivity on the Anode Electrode/Porous Transport Layer Interfacial Resistance in PEM Water Electrolyzers, J. Electrochem. Soc. 168 (2021) 084513, https://doi.org/10.1149/1945-7111/AC1EB4.

[11] D. Hoffmeister, S. Finger, L. Fiedler, T.-C. Ma, A. Körner, M. Zlatar, B. Fritsch, K. W. Bodnar, S. Carl, A. Götz, B.A. Zubiri, J. Will, E. Spiecker, S. Cherevko, A.T. S. Freiberg, K.J.J. Mayrhofer, S. Thiele, A. Hutzler, C. van Pham, Photodeposition-Based Synthesis of TiO2@IrOx Core–Shell Catalyst for Proton Exchange Membrane Water Electrolysis with Low Iridium Loading, Adv. Sci. 11 (2024) 2402991, https://doi.org/10.1002/advs.202402991.

[12] T. Schuler, R. De Bruycker, T.J. Schmidt, F.N. Büchi, Polymer Electrolyte Water Electrolysis: Correlating Porous Transport Layer Structural Properties and Performance: Part I. Tomographic Analysis of Morphology and Topology, J. Electrochem. Soc. 166 (2019) F270, https://doi.org/10.1149/2.0561904jes.

[13] C.M. Hwang, M. Ishida, H. Ito, T. Maeda, A. Nakano, A. Kato, T. Yoshida, Effect of titanium powder loading in gas diffusion layer of a polymer electrolyte unitized reversible fuel cell, J. Power Sources 202 (2012) 108–113, https://doi.org/10.1016/j.jpowsour.2011.11.041.

[14] M. Bernt, A. Siebel, H.A. Gasteiger, Analysis of Voltage Losses in PEM Water Electrolyzers with Low Platinum Group Metal Loadings, J. Electrochem. Soc. 165 (2018) F305–F, https://doi.org/10.1149/2.0641805JES.

[15] T.-C. Ma, A. Hutzler, B. Bensmann, R. Hanke-Rauschenbach, S. Thiele, Influence of the Complex Interface between Transport and Catalyst Layer on Water Electrolysis Performance, J. Electrochem. Soc. 171 (2024) 044504, https://doi.org/10.1149/1945-7111/ad3497.

[16] C. Liu, J.A. Wrubel, E. Padgett, G. Bender, Impacts of PTL coating gaps on cell performance for PEM water electrolyzer, Appl. Energy 356 (2024) 122274, https://doi.org/10.1016/j.apenergy.2023.122274.

[17] T. Schuler, J.M. Ciccone, B. Krentscher, F. Marone, C. Peter, T.J. Schmidt, F. N. Büchi, Hierarchically Structured Porous Transport Layers for Polymer Electrolyte Water Electrolysis, Adv. Energy Mater. 10 (2020) 1903216, https://doi.org/10.1002/aenm.201903216.

[18] E. Padgett, G. Bender, A. Haug, K. Lewinski, F. Sun, H. Yu, D.A. Cullen, A. J. Steinbach, S.M. Alia, Catalyst Layer Resistance and Utilization in PEM Electrolysis, J. Electrochem. Soc. 170 (2023) 084512, https://doi.org/10.1149/1945-7111/acee25.

[19] A. Hartig-Weiß, M. Bernt, A. Siebel, H.A. Gasteiger, A Platinum Micro-Reference Electrode for Impedance Measurements in a PEM Water Electrolysis Cell, J. Electrochem. Soc. 168 (2021) 114511, https://doi.org/10.1149/1945-7111/ac3717.

[20] T. Schuler, C.C. Weber, J.A. Wrubel, L. Gubler, B. Pivovar, F.N. Büchi, G. Bender, Ultrathin Microporous Transport Layers: Implications for Low Catalyst Loadings, Thin Membranes, and High Current Density Operation for Proton Exchange Membrane Electrolysis, Adv. Energy Mater. 14 (2024) 2302786, https://doi.org/10.1002/aenm.202302786.

[21] M.F. Ernst, V. Meier, M. Kornherr, H.A. Gasteiger, Preparation and Performance Evaluation of Microporous Transport Layers for Proton Exchange Membrane (PEM) Water Electrolyzer Anodes, J. Electrochem. Soc. 171 (2024) 074511, https://doi.org/10.1149/1945-7111/ad63cf.

[22] F. Hegge, F. Lombeck, E. Cruz Ortiz, L. Bohn, M. von Holst, M. Kroschel, J. Hübner, M. Breitwieser, P. Strasser, S. Vierrath, Efficient and Stable Low Iridium Loaded Anodes for PEM Water Electrolysis Made Possible by Nanofiber Interlayers, ACS Appl. Energy Mater. 3 (2020) 8276–8284, https://doi.org/10.1021/acsaem.0c00735.

[23] G. Lodi, A. De Battisti, G. Bordin, C. De Asmundis, A. Benedetti, Microstructure and electrical properties of IrO2 prepared by thermal decomposition of IrCl3·x H2O: Role played by the conditions of thermal treatment, J. Electroanal. Chem. Interfacial Electrochem. 277 (1990) 139–150, https://doi.org/10.1016/0022-0728(90)85096-N.

[24] G. Doo, J. Park, J. Park, J. Heo, J. Jung, D.W. Lee, H. Bae, J. Hyun, E. Oh, J. Kwen, K.M. Kim, H.-T. Kim, Contact Problems of IrOx Anodes in Polymer Electrolyte Membrane Water Electrolysis, ACS Energy Lett. 8 (2023) 2214–2220, https://doi.org/10.1021/acsenergylett.3c00291.

[25] S. Geiger, O. Kasian, A.M. Mingers, S.S. Nicley, K. Haenen, K.J.J. Mayrhofer, S. Cherevko, Catalyst Stability Benchmarking for the Oxygen Evolution Reaction: The Importance of Backing Electrode Material and Dissolution in Accelerated Aging Studies, ChemSusChem 10 (2017) 4140–4143, https://doi.org/10.1002/cssc.201701523.

[26] M. Zlatar, D. Escalera-López, M.G. Rodríguez, T. Hrbek, C. Götz, R. Mary Joy, A. Savan, H.P. Tran, H.N. Nong, P. Pobedinskas, V. Briega-Martos, A. Hutzler, T. Böhm, K. Haenen, A. Ludwig, I. Khalakhan, P. Strasser, S. Cherevko, Standardizing OER Electrocatalyst Benchmarking in Aqueous Electrolytes: Comprehensive Guidelines for Accelerated Stress Tests and Backing Electrodes, ACS Catal. 13 (2023) 15375–15392, https://doi.org/10.1021/acscatal.3c03880.

[27] D.Y. Chung, S. Park, P.P. Lopes, V.R. Stamenkovic, Y.-E. Sung, N.M. Markovic, D. Strmcnik, Electrokinetic Analysis of Poorly Conductive Electrocatalytic Materials, ACS Catal. 10 (2020) 4990–4996, https://doi.org/10.1021/acscatal.0c00960.

[28] J. Schröder, V.A. Mints, A. Bornet, E. Berner, M. Fathi Tovini, J. Quinson, G.K. H. Wiberg, F. Bizzotto, H.A. El-Sayed, M. Arenz, The Gas Diffusion Electrode Setup as Straightforward Testing Device for Proton Exchange Membrane Water Electrolyzer Catalysts, JACS Au 1 (2021) 247–251, https://doi.org/10.1021/jacsau.1c00015.

[29] P. Collantes Jiménez, G.K.H. Wiberg, G.W. Sievers, V. Brüser, M. Arenz, Bridging the gap between basic research and application: a half-cell setup for high current density measurements of Ir-based oxygen evolution reaction catalysts on porous transport electrodes, J. Mater. Chem. A 11 (2023) 20129–20138, https://doi.org/10.1039/D3TA04136K.

[30] M. Geuß, L. Löttert, T. Böhm, A. Hutzler, K.J.J. Mayrhofer, S. Thiele, S. Cherevko, Quantification of Iridium Dissolution at Water Electrolysis Relevant Conditions Using a Gas Diffusion Electrode Half-Cell Setup, ACS Catal. 14 (2024) 11819–11831, https://doi.org/10.1021/acscatal.4c02159.

[31] B. Mayerhöfer, D. McLaughlin, T. Böhm, M. Hegelheimer, D. Seeberger, S. Thiele, Bipolar Membrane Electrode Assemblies for Water Electrolysis, ACS Appl. Energy Mater. 3 (2020) 9635–9644, https://doi.org/10.1021/acsaem.0c01127.

[32] M. Bühler, F. Hegge, P. Holzapfel, M. Bierling, M. Suermann, S. Vierrath, S. Thiele, Optimization of anodic porous transport electrodes for proton exchange membrane water electrolyzers, J. Mater. Chem. A 7 (2019) 26984–26995, https://doi.org/10.1039/c9ta08396k.

[33] K. Ehelebe, D. Seeberger, M.T.Y. Paul, S. Thiele, K.J.J. Mayrhofer, S. Cherevko, Evaluating Electrocatalysts at Relevant Currents in a Half-Cell: The Impact of Pt Loading on Oxygen Reduction Reaction, J. Electrochem. Soc. 166 (2019) F1259–F1268, https://doi.org/10.1149/2.0911915jes.

[34] M. Geuß, M. Milosevic, M. Bierling, L. Löttert, D. Abbas, D. Escalera-López, V. Lloret, K. Ehelebe, K.J.J. Mayrhofer, S. Thiele, S. Cherevko, Investigation of Iridium-Based OER Catalyst Layers in a GDE Half-Cell Setup: Opportunities and Challenges, J. Electrochem. Soc. 170 (2023) 114510, https://doi.org/10.1149/1945-7111/ad07ac.

[35] A. Hutzler, C.D. Matthus, M. Rommel, L. Frey, Generalized approach to design multi-layer stacks for enhanced optical detectability of ultrathin layers, Appl. Phys. Lett. 110 (2017) 021909, https://doi.org/10.1063/1.4973968.

[36] A. Hutzler, C.D. Matthus, C. Dolle, M. Rommel, M.P.M. Jank, E. Spiecker, L. Frey, Large-Area Layer Counting of Two-Dimensional Materials Evaluating the Wavelength Shift in Visible-Reflectance Spectroscopy, J. Phys. Chem. C 123 (2019) 9192–9201, https://doi.org/10.1021/acs.jpcc.9b00957.

[37] A. Hutzler, B. Fritsch, C.D. Matthus, M.P.M. Jank, M. Rommel, Highly accurate determination of heterogeneously stacked Van-der-Waals materials by optical microspectroscopy, Sci. Rep. 10 (2020) 13676, https://doi.org/10.1038/s41598-020-70580-3.

[38] J. Schwarz, M. Niebauer, M. Koleśnik-Gray, M. Szabo, L. Baier, P. Chava, A. Erbe, V. Krstić, M. Rommel, A. Hutzler, Correlating Optical Microspectroscopy with 4×4 Transfer Matrix Modeling for Characterizing Birefringent Van der Waals Materials, Small Methods 7 (2023) 2300618, https://doi.org/10.1002/smtd.202300618.
[39] E.R. Peck, K. Reeder, Dispersion of Air, J. Opt. Soc. Am. 62 (1972) 958–962, https://doi.org/10.1364/JOSA.62.000958.
[40] M.A. Green, Self-consistent optical parameters of intrinsic silicon at 300K including temperature coefficients, Sol. Energy Mater. Sol. Cells 92 (2008) 1305–1310, https://doi.org/10.1016/j.solmat.2008.06.009.
[41] L. Gao, F. Lemarchand, M. Lequime, Refractive index determination of SiO2 layer in the UV/Vis/NIR range: spectrophotometric reverse engineering on single and bi-layer designs, J. Eur. Opt. Soc.-Rapid Publ. 8 (2013), https://doi.org/10.2971/jeos.2013.13010.
[42] D.P. Kulikova, A.A. Dobronosova, V.V. Kornienko, I.A. Nechepurenko, A. S. Baburin, E.V. Sergeev, E.S. Lotkov, I.A. Rodionov, A.V. Baryshev, A. V. Dorofeenko, Optical properties of tungsten trioxide, palladium, and platinum thin films for functional nanostructures engineering, Opt. Express 28 (2020) 32049–32060, https://doi.org/10.1364/OE.405403.
[43] E.D. Palik, Handbook of optical constants of solids, Academic Press, 1991.
[44] M. Bierling, D. McLaughlin, B. Mayerhöfer, S. Thiele, Toward Understanding Catalyst Layer Deposition Processes and Distribution in Anodic Porous Transport Electrodes in Proton Exchange Membrane Water Electrolyzers, Adv. Energy Mater. 13 (2023) 2203636, https://doi.org/10.1002/aenm.202203636.
[45] Y. Matsumoto, E. Sato, Electrocatalytic properties of transition metal oxides for oxygen evolution reaction, Mater. Chem. Phys. 14 (1986) 397–426, https://doi.org/10.1016/0254-0584(86)90045-3.
[46] T. Reier, D. Teschner, T. Lunkenbein, A. Bergmann, S. Selve, R. Kraehnert, R. Schlögl, P. Strasser, Electrocatalytic Oxygen Evolution on Iridium Oxide: Uncovering Catalyst-Substrate Interactions and Active Iridium Oxide Species, J. Electrochem. Soc. 161 (2014) F876–F882, https://doi.org/10.1149/2.0411409JES/XML.
[47] A.C. Lazanas, M.I. Prodromidis, Electrochemical Impedance Spectroscopy—A Tutorial, ACS Measurement Science Au 3 (2023) 162–193, https://doi.org/10.1021/acsmeasuresciau.2c00070.
[48] J. Landesfeind, J. Hattendorff, A. Ehrl, W.A. Wall, H.A. Gasteiger, Tortuosity Determination of Battery Electrodes and Separators by Impedance Spectroscopy, J. Electrochem. Soc. 163 (2016) A1373, https://doi.org/10.1149/2.1141607jes.
[49] A.S. Keefe, S. Buteau, I.G. Hill, J.R. Dahn, Temperature Dependent EIS Studies Separating Charge Transfer Impedance from Contact Impedance in Lithium-Ion Symmetric Cells, J. Electrochem. Soc. 166 (2019) A3272, https://doi.org/10.1149/2.0541914jes.
[50] M. Gaberscek, J. Moskon, B. Erjavec, R. Dominko, J. Jamnik, The Importance of Interphase Contacts in Li Ion Electrodes: The Meaning of the High-Frequency Impedance Arc, Electrochem. Solid-State Lett. 11 (2008) A170, https://doi.org/10.1149/1.2964220.
[51] S. Fletcher, The two-terminal equivalent network of a three-terminal electrochemical cell, Electrochem. Commun. 3 (2001) 692–696, https://doi.org/10.1016/S1388-2481(01)00233-8.
[52] BioLogic Science Instruments, Equivalent model of an electrochemical cell including the reference electrode impedance and the potentiostat parasitics https://www.biologic.net/documents/eis-artifacts-precautions-electrochemistry-battery-application-note-44/ (accessed 20 January 2025).
[53] L.H. Brickwedde, Properties of aqueous solutions of perchloric acid, J. Res. Nat. Bur. Stand. 42 (1949) 309, https://doi.org/10.6028/JRES.042.026.
[54] Gamry Instruments EIS of Difficult Samples. https://www.gamry.com/assets/uploads/resources/EIS-Difficult-Samples.pdf (accessed 20 January 2025).
[55] G. Doo, H. Bae, J. Park, J. Hyun, I. Kim, D.W. Lee, E. Oh, H.-T. Kim, Designing a Schottky Barrier-Free Interface for a Highly Conductive Anode in Proton Exchange Membrane Water Electrolysis, ACS Nano 18 (2024) 23331–23340, https://doi.org/10.1021/acsnano.4c06373.
[56] D. Kulkarni, A. Huynh, P. Satjaritanun, M. O'Brien, S. Shimpalee, D. Parkinson, P. Shevchenko, F. DeCarlo, N. Danilovic, K.E. Ayers, C. Capuano, I.V. Zenyuk, Elucidating effects of catalyst loadings and porous transport layer morphologies on operation of proton exchange membrane water electrolyzers, Appl. Catal., B 308 (2022) 121213, https://doi.org/10.1016/J.APCATB.2022.121213.
[57] R. Makharia, M.F. Mathias, D.R. Baker, Measurement of Catalyst Layer Electrolyte Resistance in PEFCs Using Electrochemical Impedance Spectroscopy, J. Electrochem. Soc. 152 (2005) A970, https://doi.org/10.1149/1.1888367.
[58] Y.-S. Li, D. Menga, H.A. Gasteiger, B. Suthar, Design of PGM-Free Cathode Catalyst Layers for PEMFC Applications: The Impact of Electronic Conductivity, J. Electrochem. Soc. 170 (2023) 094503, https://doi.org/10.1149/1945-7111/acf1d3.
[59] O. Kasian, S. Geiger, T. Li, J.-P. Grote, K. Schweinar, S. Zhang, C. Scheu, D. Raabe, S. Cherevko, B. Gault, K.J.J. Mayrhofer, Degradation of iridium oxides via oxygen evolution from the lattice: correlating atomic scale structure with reaction mechanisms, Energy Environ. Sci. 12 (2019) 3548–3555, https://doi.org/10.1039/C9EE01872G.
[60] N. Danilovic, R. Subbaraman, K.-C. Chang, S.H. Chang, Y.J. Kang, J. Snyder, A. P. Paulikas, D. Strmcnik, Y.-T. Kim, D. Myers, V.R. Stamenkovic, N.M. Markovic, Activity–Stability Trends for the Oxygen Evolution Reaction on Monometallic Oxides in Acidic Environments, J. Phys. Chem. Lett. 5 (2014) 2474–2478, https://doi.org/10.1021/jz501061n.
[61] L.V. Bühre, S. Bullerdiek, P. Trinke, B. Bensmann, A.-L.-E.-R. Deutsch, P. Behrens, R. Hanke-Rauschenbach, Application and Analysis of a Salt Bridge Reference Electrode Setup for PEM Water Electrolysis: Towards an Extended Voltage Loss Break Down, J. Electrochem. Soc. 169 (2022) 124513, https://doi.org/10.1149/1945-7111/ac9ee1.
[62] J. Nicholls, S. Dimitrijev, P. Tanner, J. Han, Description and Verification of the Fundamental Current Mechanisms in Silicon Carbide Schottky Barrier Diodes, Sci. Rep. 9 (2019) 3754, https://doi.org/10.1038/s41598-019-40287-1.
[63] R.C. Rossi, N.S. Lewis, Investigation of the Size-Scaling Behavior of Spatially Nonuniform Barrier Height Contacts to Semiconductor Surfaces Using Ordered Nanometer-Scale Nickel Arrays on Silicon Electrodes, J. Phys. Chem. B 105 (2001) 12303–12318, https://doi.org/10.1021/jp011861c.
[64] M.G. Walter, E.L. Warren, J.R. McKone, S.W. Boettcher, Q. Mi, E.A. Santori, N. S. Lewis, Solar Water Splitting Cells, Chem. Rev. 110 (2010) 6446–6473, https://doi.org/10.1021/cr1002326.
[65] H.L. Tan, F.F. Abdi, Y.H. Ng, Heterogeneous photocatalysts: an overview of classic and modern approaches for optical, electronic, and charge dynamics evaluation, Chem. Soc. Rev. 48 (2019) 1255–1271, https://doi.org/10.1039/C8CS00882E.
[66] B. Mei, T. Pedersen, P. Malacrida, D. Bae, R. Frydendal, O. Hansen, P.C.K. Vesborg, B. Seger, I. Chorkendorff, Crystalline TiO2: A Generic and Effective Electron-Conducting Protection Layer for Photoanodes and -cathodes, J. Phys. Chem. C 119 (2015) 15019–15027, https://doi.org/10.1021/acs.jpcc.5b04407.
[67] M.Z. Musa, M.S.P. Sarah, S.S. Shariffudin, M.H. Mamat, M. Rusop, A study on ohmic contact of different metal contact materials on nanostructured Titanium Dioxide (TiO2) Thin Film, in: 2010 International Conference on Electronic Devices, Systems and Applications, 11-14 April 2010, 2010, pp. 412–414, https://doi.org/10.1109/ICEDSA.2010.5503028.
[68] F. Ebadi, N. Taghavinia, R. Mohammadpour, A. Hagfeldt, W. Tress, Origin of apparent light-enhanced and negative capacitance in perovskite solar cells, Nat. Comm. 10 (2019) 1574, https://doi.org/10.1038/s41467-019-09079-z.
[69] K. Miyano, M. Yanagida, N. Tripathi, Y. Shirai, Simple characterization of electronic processes in perovskite photovoltaic cells, Appl. Phys. Lett. 106 (2015) 093903, https://doi.org/10.1063/1.4914086.
[70] Y.W. Chen, J.D. Prange, S. Dühnen, Y. Park, M. Gunji, C.E.D. Chidsey, P. C. McIntyre, Atomic layer-deposited tunnel oxide stabilizes silicon photoanodes for water oxidation, Nat. Mater. 10 (2011) 539–544, https://doi.org/10.1038/nmat3047.
[71] R. Kötz, H. Neff, S. Stucki, Anodic Iridium Oxide Films: XPS-Studies of Oxidation State Changes and, J. Electrochem. Soc. 131 (1984) 72, https://doi.org/10.1149/1.2115548.
[72] C.V. Pham, M. Bühler, J. Knöppel, M. Bierling, D. Seeberger, D. Escalera-López, K. J.J. Mayrhofer, S. Cherevko, S. Thiele, IrO2 coated TiO2 core-shell microparticles advance performance of low loading proton exchange membrane water electrolyzers, Appl. Catal., B 269 (2020) 118762, https://doi.org/10.1016/j.apcatb.2020.118762.
[73] S. Trasatti, O.A. Petrii, Real surface area measurements in electrochemistry, J. Electroanal. Chem. 327 (1992) 353–376, https://doi.org/10.1016/0022-0728(92)80162-W.
[74] J. Semple, D.G. Georgiadou, G. Wyatt-Moon, G. Gelinck, T.D. Anthopoulos, Flexible diodes for radio frequency (RF) electronics: a materials perspective, Semicond. Sci. Technol. 32 (2017) 123002, https://doi.org/10.1088/1361-6641/aa89ce.
[75] C.W. Wilmsen, Physics and chemistry of III-V compound semiconductor interfaces (in English), Plenum Press, New York, NY, 1985.
[76] J.J. Yang, N.P. Kobayashi, J.P. Strachan, M.X. Zhang, D.A.A. Ohlberg, M.D. Pickett, Z. Li, G. Medeiros-Ribeiro, R.S. Williams, Dopant Control by Atomic Layer Deposition in Oxide Films for Memristive Switches, Chem. Mater. 23 (2011) 123–125, https://doi.org/10.1021/cm1020959.
[77] V.L. Rideout, A review of the theory and technology for ohmic contacts to group III–V compound semiconductors, Solid State Electron. 18 (1975) 541–550, https://doi.org/10.1016/0038-1101(75)90031-3.
[78] F.A. Padovani, R. Stratton, Field and thermionic-field emission in Schottky barriers, Solid State Electron. 9 (1966) 695–707, https://doi.org/10.1016/0038-1101(66)90097-9.
[79] B.L. Sharma, Metal-Semiconductor Schottky Barrier Junctions and Their Applications, Springer, New York, 1984.
[80] S. Yan, K.P. Abhilash, L. Tang, M. Yang, Y. Ma, Q. Xia, Q. Guo, H. Xia, Research Advances of Amorphous Metal Oxides in Electrochemical Energy Storage and Conversion, Small 15 (2019) 1804371, https://doi.org/10.1002/smll.201804371.
[81] S.A. Berlinger, X. Peng, X. Luo, P.J. Dudenas, G. Zeng, H. Yu, D.A. Cullen, A. Z. Weber, N. Danilovic, A. Kusoglu, Iridium Surface Oxide Affects the Nafion Interface in Proton-Exchange-Membrane Water Electrolysis, ACS Energy Lett. (2024) 4792–4799, https://doi.org/10.1021/acsenergylett.4c01508.
[82] R. Girod, T. Lazaridis, H.A. Gasteiger, V. Tileli, Three-dimensional nanoimaging of fuel cell catalyst layers, Nat. Catal. 6 (2023) 383–391, https://doi.org/10.1038/s41929-023-00947-y.
[83] A. Atkinson, Transport processes during the growth of oxide films at elevated temperature, Rev. Mod. Phys. 57 (1985) 437–470, https://doi.org/10.1103/RevModPhys.57.437.
[84] J.J. Yang, J.P. Strachan, F. Miao, M.-X. Zhang, M.D. Pickett, W. Yi, D.A.A. Ohlberg, G. Medeiros-Ribeiro, R.S. Williams, Metal/TiO2 interfaces for memristive switches, Appl. Phys. A 102 (2011) 785–789, https://doi.org/10.1007/s00339-011-6265-8.
[85] O. Kasian, J.-P. Grote, S. Geiger, S. Cherevko, K.J.J. Mayrhofer, The Common Intermediates of Oxygen Evolution and Dissolution Reactions during Water Electrolysis on Iridium, Angew. Chem. Int. Ed. 57 (2018) 2488–2491, https://doi.org/10.1002/ANIE.201709652.
[86] K. Sun, X. Liang, X. Wang, Y.A. Wu, S. Jana, Y. Zou, X. Zhao, H. Chen, X. Zou, Highly Efficient and Durable Anode Catalyst Layer Constructed with Deformable

Hollow IrOx Nanospheres in Low-Iridium PEM Water Electrolyzer, Angew. Chem. Int. Ed. (2025) e202504531, https://doi.org/10.1002/anie.202504531.